TWO-DIMENSIONAL COBALT-PLATINUM NANOFRAMES: SYNTHESIS, STRUCTURE, AND ELECTROCHEMICAL OXYGEN REDUCTION ACTIVITY

by

Yuanfang Ying, M.S.

A thesis submitted to the Graduate Council of
Texas State University in partial fulfillment
of the requirements for the degree of
Master of Science
with a Major in Chemistry
August 2017

Committee Members:

Christopher Rhodes, Chair

Benjamin Martin

Jennifer Irvin

FAIR USE AND AUTHOR'S PERMISSION STATEMENT

Fair Use

Duplication Permission

ACKNOWLEDGEMENTS

This work was supported by the Office of Naval Research (N00014-16-1-2777) and the National Science Foundation PREM (DMR-1205670). The author would like to thank to Fernando Godinez-Salomon and Christopher P. Rhodes who contributed to this work. Thesis committee members to be recognized for significant constructive input are Benjamin Martin, Jennifer Irvin and most of all Christopher P. Rhodes.

TABLE OF CONTENTS

Page

LIST OF TABLES

Table **Page**

LIST OF FIGURES

Figure **Page**

LIST OF ABBREVIATIONS

Abbreviation	Description
PEMFCs	Proton exchange membrane fuel cells
ORR	Oxygen reduction reaction
2D	Two-dimensional
EG	Ethylene glycol
BET	Brunauer–Emmett–Teller
RDE	Rotating disk electrode
CV	Cyclic voltammetry
CO stripping	Carbon monoxide stripping
XRD	X-ray powder diffraction
SEM	Scanning electron microscope
EDS	Energy dispersive X-ray spectroscopy
TEM	Transmission electron microscopy
TGA	Thermogravimetric analysis
ECSA	Electrochemical surface area
H_{upd}	Hydrogen underpotential deposition

ABSTRACT

Proton exchange membrane (PEM) fuel cells which convert hydrogen and oxygen to electricity have attracted significant attention due to their high efficiency and clean byproducts. Electrochemical Oxygen Reduction Reaction (ORR) catalysts with high activity and improved stability are needed. Catalyst stability at elevated potentials is a particularly important and unsolved problem. Most commonly used ORR catalysts are carbon-supported platinum (Pt)/Pt-alloys. However, carbon degradation occurs at high electrochemical potentials resulting in performance degradation of the catalyst. This project evaluated the synthesis, structure, and properties of Co-Pt two-dimensional nanoframes which act as carbon-free ORR catalysts. The Co-Pt 2D nanoframes catalysts were synthesised using a three-step process: (i) synthesis of cobalt hydroxide nanosheets with high surface area, (ii) deposition of Pt onto the cobalt hydroxide nanosheets, and (iii) heat treatment under reducing conditions to facilitate interation of Co and Pt. The ORR specific and mass activity of Co-Pt-200 were determined to be 8 and 3 times higher than Pt/C, respectively. The ORR activities are higher than any activities of Co-Pt reported to date. The effects of thermal treatment temperature and adding a third transition metal on the ORR catalytic activity were also evaluated.

1. INTRODUCTION

1.1 Fuel Cells: Background and Research Needs

Due to economic growth and population expansion, energy consumption is increasing and dependence on carbon-based fuels is continuing.[1] Figure 1 shows that approximately 76% of the global energy supplies come from non-renewable, carbon-releasing fossil fuels, whereas around 24% of the global energy supply is combustible and renewable.[2] The environmental issues caused by combustion of carbon-based fuels are more and more serious. Thus, significant efforts have been devoted to the development of alternatives to conventional energy supplies. So far, the choice of alternatives is based on accessibility, renewability, and effect on the environment.[1]

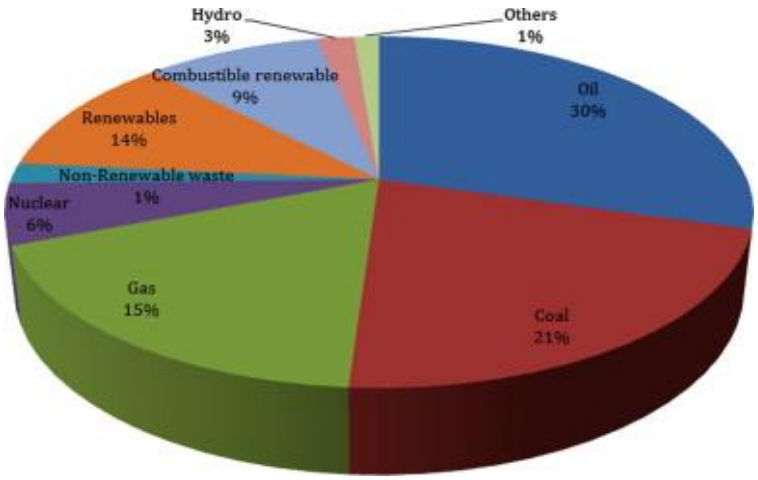

Figure 1. Share of world primary energy supply 2008. [2]

For the past few decades, studies have focused on fuel cell technologies including, proton exchange membrane (PEM) fuel cells which efficiently convert hydrogen and oxygen to clean electricity.[2] Figure 2 shows the electrode reactions and charge flow for the fuel cell in acidic conditions. The overall reaction is $H_2 + ½O_2 \rightarrow H_2O$. At the anode of an acidic PEM fuel cell, hydrogen gas is oxidized, releasing electrons which are passed

through an electrical circuit to the cathode and H^+ which is transported through the electrolyte.

$$2H_2 \rightarrow 4H^+ + 4e^- \quad (1)$$

At the cathode, oxygen reduction occurs by oxygen reacting with electrons from the anode, and H^+ ions from the electrolyte, to form water.

$$O_2 + 4e^- + 4H^+ \rightarrow 2H_2O \quad (2)$$

Significant efforts are needed to develop oxygen reduction reaction (ORR) catalyst with improved activity and stability, and lower cost.[3, 4]

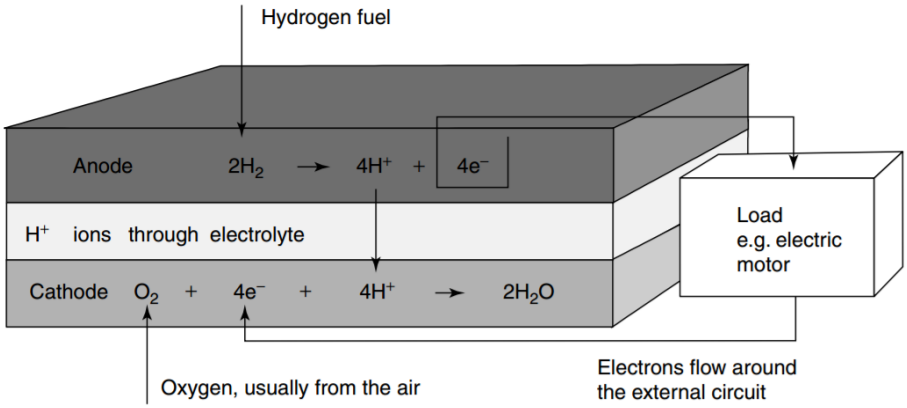

Figure 2. Electrode reactions and charge flow for an acid electrolyte fuel cell.[5]

1.2 Oxygen Reduction Reaction in Acid Electrolyte

In the oxygen reduction reaction, there are two types of adsorption of O_2 on the catalyst surfaces: bidentate O_2 adsorption (two O atoms coordinate with the catalyst) and end-on O_2 adsorption (one O atom coordinates perpendicularly to the catalyst).[6] Depending on the type of oxygen adsorption, there are mainly two pathways for ORR in aqueous solutions: the direct 4-electron oxygen reduction pathway that converts O_2 to H_2O, and the 2-electron oxygen reduction pathway that transfer O_2 to hydrogen peroxide (H_2O_2).[7, 8]

Table 1 provides several typical ORR processes with their corresponding thermodynamic electrode potentials under standard conditions. The electrode potential depends on the catalyst and the electrolyte.

Table 1. Thermodynamic electrode potentials of electrochemical O_2 reductions. [9]

Electrolyte	ORR reactions	Thermodynamic electrode potential at standard conditions, V
Acidic aqueous solution	$O_2 + 4H^+ + 4e^- \rightarrow H_2O$	1.229
	$O_2 + 2H^+ + 2e^- \rightarrow H_2O_2$	0.70
	$H_2O_2 + 2H^+ + 2e^- \rightarrow 2H_2O$	1.76

The ORR proceeds by four primary steps (i) O_2 diffusion, (ii) adsorption of O_2 onto a catalyst surface, (iii) electrons (from the anode side) are transferred to the adsorbed oxygen, weakening and breaking the oxygen double bond, and (iv) hydroxide ions react to produce H_2O which is removed from the catalyst surface.[10] Normally, the ORR kinetics is very slow. A cathode ORR catalyst is needed to speed up the ORR kinetics to reach a practically usable level.

In addition, the surface area of an electrode is an important parameter which is very important to fuel cells. For ORR, O_2 gas and H^+ ions from the electrolyte, as well as the necessary activation energy must come together on the surface of an electrode, and the water produced must be removed. This is called the three phases boundary. Thus, the design and manufacture of a fuel cell electrode with a large surface area is therefore a very important issue for practical fuel cells.[5]

Furthermore, ORR catalysts must be stable at high potentials in a corrosive environment. Enhanced long term stability of the catalyst is another critical consideration.

1.3 Electrocatalysts for Oxygen Reduction Reaction

1.3.1 Platinum (Pt)

Pt is the most commonly used metal for ORR catalyst. Pt catalytic ORR has a multi-electron pathway in both acid and alkaline electrolytes,[12] including several elementary steps and reaction intermediates. The simplified mechanism is shown in Figure 3.

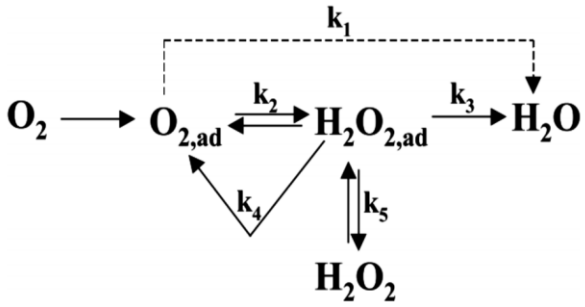

Figure 3. The oxygen reduction reaction mechanism on Pt. [12]

The thermodynamic potential of ORR (1.23 V vs. NHE at standard conditions) is so high that Pt electrode undergoes oxidation, which changes its surface structure. At high potential, the reaction is as follows:

$$Pt + 1/2O_2 = PtO \qquad E^o = 0.88\ V \qquad (3)$$

Therefore, the observed potential is normally lower than 1.23 V. The potential of a Pt electrode in O_2 saturated 1 M H_2SO_4 is 1.06 V, which is a mixed value of the thermodynamic potential of Pt oxidation and O_2 reduction.[13] Furthermore, the kinetics of O_2 reduction on Pt is not the same at different potential ranges.[14]

The catalytic activity of Pt towards ORR strongly depends on its O_2 adsorption energy, the dissociation energy of the O-O bond, and the binding energy of OH on the surface.[15] Thus, the Pt catalyst needs to counterbalance two opposing effects, a relatively strong adsorption energy of O_2 and intermediates O_2^-, O_2^{2-}, H_2O_2, etc. and a relatively low

adsorption of spectator oxygenated species OH, etc. and specifically adsorbed anions onto active sites.[16, 17]

Recent studies have shown that the rate-determining step is the first electron transfer to $O_{2,ad}$. The rate expression is,[72]

$$i = nFKc_{O_2}(1-\Theta_{ad})^x \exp(-\beta FE/RT)\exp(-\gamma \Delta G_{ad}/RT) \qquad (4)$$

where n, F, K, c_{O_2}, R, x, β and γ are constants, E is the electrode potential, T is the temperature and Θ_{ad} is the total surface coverage by spectator species and ΔG_{ad} is the Gibbs energy of adsorption of reactive intermediates.

Various factors have been proposed that will affect these parameters, including, the electronic structure of the Pt catalyst (Pt d-band vacancy),[19] Pt d-band center downshifting, and the Pt-Pt interatomic distance (geometric effect).[18, 20] In addition, the ORR behaviors of Pt have a relationship with Pt surfaces. At low index Pt surfaces, including Pt (111), Pt (100), and Pt (110), the ORR have been extensively studied.[21, 22] The principal conclusion is that the activity of ORR in $HClO_4$ solution follows the order of Pt (100) ≪ Pt (111) ≈ Pt (110).

As shown in Figure 4, Pt is a scarce and expensive metal.[11] However, high Pt loadings (~0.4 mg cm^{-2}) are needed to achieve a satisfying fuel cell performance in the practical application. Therefore, many studies have been focused on the development of catalysts with reducing Pt loading or even completely using an abundant and cheap metal instead of Pt.

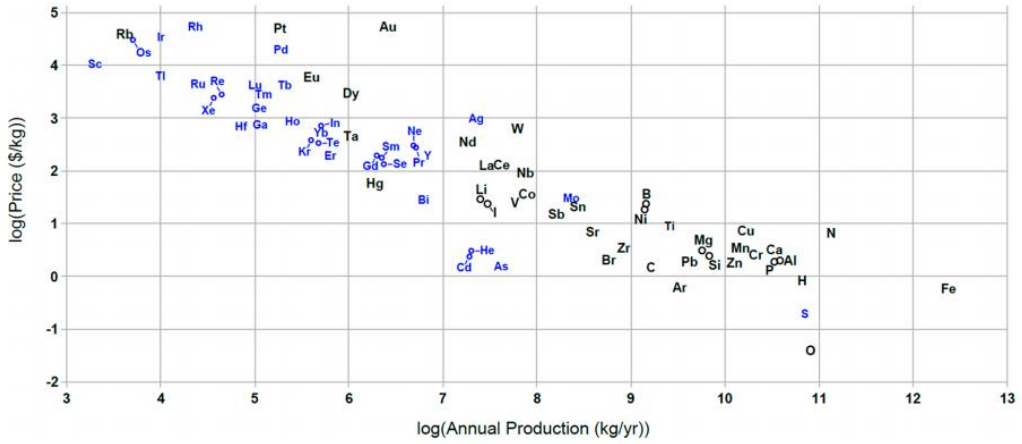

Figure 4. Price of the elements (in $/kg) versus their annual production (in kg/yr).[11]

1.3.2 Pt-Nonnoble Transition Metal Alloys

Typically, in a PEM cell, Pt-based electrocatalysts and their associated catalysts layers contribute over 55% of the total cost.[37] Thus, reducing the Pt loading without decreasing fuel cell performance and enhancing catalytic activity and stability is an ideal strategy for fuel cell development. Various studies show that when Pt is alloyed with other metals, the catalytic activity is enhanced. [23] The enhancement has been mainly attributed to electronic structure and geometric effects.

Stamenkovic *et al*. studied the role of 3d transition metals in the ORR activity of Pt-alloys. They synthesized polycrystalline alloy films of Pt_3M catalysts (M: Ni, Co, Fe, and Ti) and found that the catalytic activity for the ORR on Pt_3M alloys is dependent on the nature of the 3d metal.[23] They also summarized a relationship in electrocatalytic trends on Pt_3M (M: Ni, Co, Fe, Ti, V) surfaces between the experimentally determined the d-band center and activity for ORR, as shown in Figure 5, this relationship exhibited a volcano-type behavior.

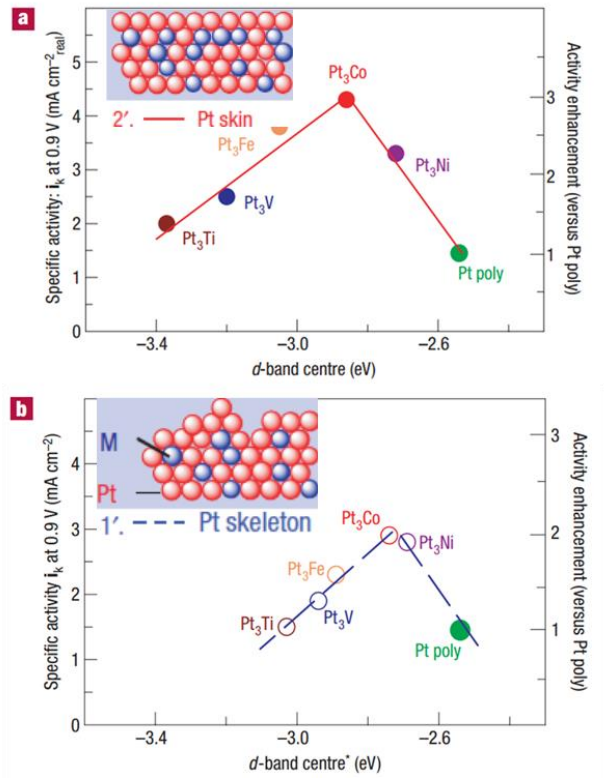

Figure 5. Relationships between the catalytic properties and electronic structure of Pt_3M alloys (a) surfaces and (b) Pt-skeleton. [23]

They also found that the arrangement of Pt on the surface region of metal support has strongly effect on the ORR kinetics. For example, in Figure 5, Pt_3Ni and Pt_3Co have a Pt-skeleton surface and Pt-skin surface, respectively. Due to the thermodynamics of surface segregation, annealed alloy surfaces could form the outermost Pt surface layer (Pt-skin surface). When these two materials were exposed to the acidic environment, the Pt-skin surface material was very stable in terms of physicochemical properties.[48, 49] However, for the Pt-skeleton surface material, transition metal atoms in the surface layer could be dissolved.[50, 51]

Ternary Pt-alloys also have been studied. For example, Wang *et al*. reported that adding a third element to the binary Pt-alloy can fine tune and optimize the d-band center

and improve the ORR activity.[65] Mani *et al*. study synergistic effects of a third metal (M=Co, Cu, Fe, Cr) in ternary $PtNi_3M$ catalysts. The results show that the interaction of Co and Cu can provide 1.7 times specific activity improvement for ORR compare with binary $Pt_{25}Ni_{75}$ catalyst.[94] However, the main challenge result from the different redox potentials of the various metals and metal precursors hinder the systematically study of ternary Pt-alloys. Furthermore, it is even more challenging to maintain the morphology of the alloy nanocrystals.[66]

1.3.3 Mechanism of Pt Alloy as catalyst

Mukerjee *et al*. proposed the enhancement mechanism on supported Pt binary alloys is the formation of favorable Pt-Pt distances. They studied the mechanism by using XANES and EXAFS and reported that d vacancy and Pt-Pt interatomic distances lead to the ORR enhancement as the plots of electronic and geometric parameters vs. electrocatalytic activity exhibit a volcano-type behavior.[63]

Density Functional Theory (DFT) calculations also have been used to investigate the performance of Pt alloys in ORR. Some DFT work has shown that modified chemisorption properties for adsorbed oxygen species on a Pt alloy surface are greatly dependent on short-range electronic charge-transfer effects (ligand effects) and long-range geometric lattice strain (geometric effects).[24-26] These electronic and geometric effects lead to a modified chemisorption of reactants, intermediates, and products.[27-29]

As shown in Figure 6, Toda *et al*. proposed that during the adsorption step in ORR, a π orbital of O_2 interacts with empty d orbitals of Pt and consequently back donation from the partially filled orbital of Pt to π^* (anti-bonding) molecular orbital of O_2. The increase in d-band vacancies on Pt by alloying produces a strong metal-O_2

interaction. This interaction weakens the O-O bonds, resulting in bond cleavage and bond formation between O and H^+ of the electrolyte. Based on equation (4), Θ_{ad} and ΔG_{ad} are decreased by alloying, thus improving the reaction rate of ORR.[30]

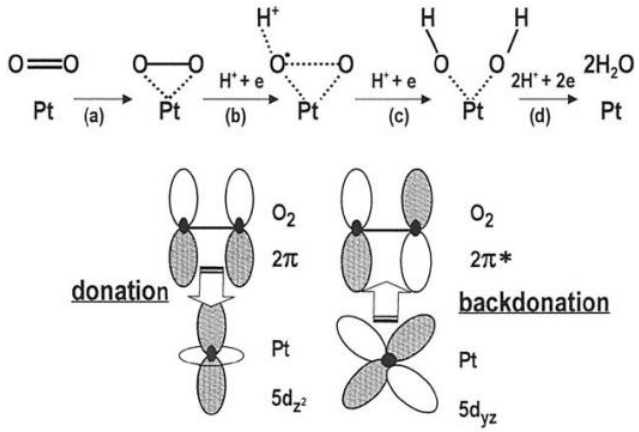

Figure 6. Schematic explanation of the proposed enhancement mechanism of the ORR by alloying Pt.[30]

Previous studies also demonstrated the catalytic activity of Pt-Ni alloys toward ORR is highly dependent on the crystal face. Stamenkovic *et al*. demonstrated that the Pt_3Ni (111) surface exhibit 10 times more active than Pt (111) for the ORR. The improvement of activity is associated with the specific electronic structure and surface atoms arrangement of the Pt_3Ni (111) surface.[98]

1.3.4 Carbon-Supported Pt Alloy Catalysts

Carbon black with high surface area has been used as the electrocatalyst support in order to improve the catalytic activity of Pt-alloy catalysts, due to their large specific surface area which can provide good a dispersion of the active component and good electric conductivity.[39,40]

Carbon supports are well-known to play a key role in improving Pt-alloy catalytic activity and stability. The carbon support may modify the electronic character, the shape and the distribution of the Pt-alloy[41], furthermore, it has been found that the carbon material also strongly influent the size, size distribution, morphology, surface structure and then effect the number of the active sites on the catalyst surface.

Wang *et al*.[44] investigated a Pt_3Co/C nanoparticle catalyst with a core-shell structure at different temperatures under a flowing $N_2(H_2)$ atmosphere. After heat treatment at 700^{o}C, the mean particle size is 5nm. The core-shell structure has ordered intermetallic cores with two to three atomic-layer Pt shells. They demonstrated that these ordered Pt_3Co/C catalysts exhibited over 200% increase in mass activity and over 300% increase in specific activity when compare with disordered Pt_3Co alloy nanoparticles and Pt/C particles.

Xiong *et al*.[0] observed higher ORR activities with the Pt-M/C (M=Fe and Co) catalysts in a PEMFC. They synthesized nanostructured Pt alloys by a microemulsion method and a mild temperature treatment. They found that the heat treatment of the catalysts at 200^{o}C in reducing atmosphere improved the catalytic activity due to the cleaning of the surface and increase in the electrochemical surface area.

However, the carbon support also has a negative impact on the catalytic activity. It may cause a severe sintering or agglomeration of Pt-alloy under long-term fuel cell operation, which leading to the decrease of electrocatalytic surface area, and then, decreasing fuel cell performance.[42,43] In addition, due to the reaction ($C + 2H_2O \rightarrow CO_2 + 4H^+ + 4e^-$) which is catalyzed by the Pt, Pt-alloys are prone to degradation during fuel cell operation, leading to loss of fuel cell performance.

Carbon degradation is enhanced and particularly a problem at elevated potentials which are encountered during start-up/shut-down, where potentials in the range of 1.3 to 1.8 V_{RHE} have been reported to occur at the cathode.[95]

Chen *et al*.[59] synthesized supportless platinum nanotubes (PtNTs) and tested the stability as catalysts for ORR in PEMFCs. As shown in Figure 7, the measurement is conducted in Ar-purged 0.5 M H_2SO_4 solution at 60 °C (0-1.3 V vs. RHE, sweep rate 50 mV s^{-1}). The cyclic voltammograms for Pt/C (20 wt% platinum on Vulcan XC-72; E-TEK) and platinum black (PtB; E-TEK) show a significant decrease of platinum ECSA, about 90 and 51% ECSA lost were observed, respectively. However, the platinum ECSA of the PtNTs only decreases about 20% as the number of cycles increases to 1000 cycles.

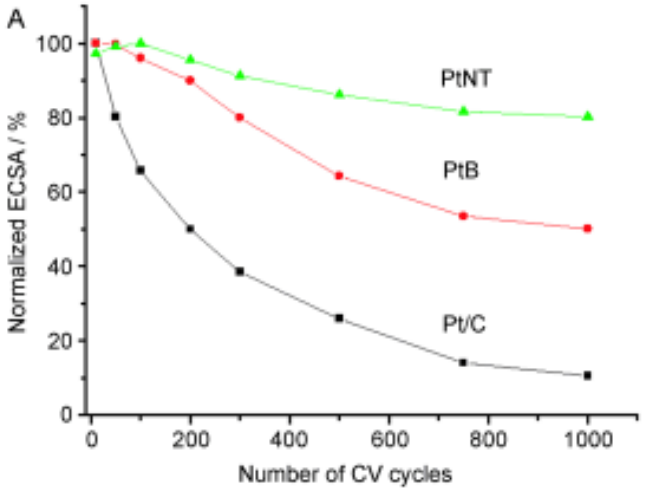

Figure 7. Loss of electrochemical surface area (ECSA) of Pt/C (E-TEK), platinum-black (PtB; E-TEK), and PtNT catalysts. [59]

1.3.5 Unsupported (Carbon Free) Pt Alloys

To address the issue of carbon supported catalyst corrosion, some alternative support and unsupported materials rather than traditional carbon support have been explored. There are some basic requirements for these noncarbon materials as fuel cell

catalysts supports, including high surface area, favored dispersion of catalytic metals, high corrosion resistance, low solubility in acidic or alkaline conditions, high electrochemical stability and high conductivity. In addition, they should have a strong physicochemical and electronic interaction with catalytic metals to change the structure of catalytic metals, then improve the activity[45, 46]. To date, these materials include metal[47, 52], oxides[53], nitride[54], carbide[55], mesoporous silicas[56] and conducting polymers[57].

Narayanamoorthy *et al*. reported that Pt_3M (M: Co, Ni and Fe) bimetallic alloy nanoclusters as a support-free electrocatalysts toward ORR. [61] Mass activities were found to be Pt-Co (0.44 $mA\mu g^{-1}$) > PtNi (0.28 $mA\mu g^{-1}$) > Pt-Fe (0.24 $mA\mu g^{-1}$) and specific activities were found to be Pt-Co (0.68 $mAcm^{-2}$) > PtNi (0.33 $mAcm^{-2}$) > Pt-Fe (0.30 $mAcm^{-2}$). In Figure 8, CV performed between 0.6 and 1.0 V_{RHE} at room temperature with 0.05 V s^{-1} scan rate. The change in ECSA after 8000 potential cycles was found to be that Pt-Co has retained 63 % of its initial ECSA and comparatively higher than Pt-Ni (48 %) and Pt-Fe (52 %).

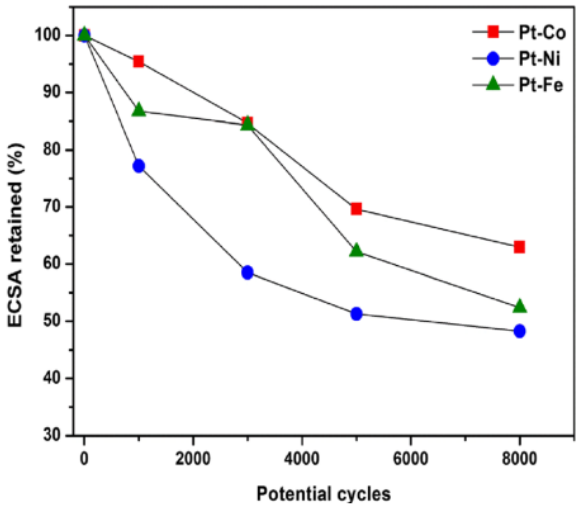

Figure 8. Normalized ECSA after accelerated durability tests.[61]

Baldizzone *et al*. prepared a representative porous nanoparticulate system and analyzed the durability of the catalyst.[61] In Figure 9. CV performed between 0.4 and 1.4 V_{RHE} at room temperature with 1.0 V s^{-1} scan rate, ECSA shows much less decrease (around 10%) in the first 1000 cycles compare with the previously mentioned Pt/C. however, ECSA and SA indeed severely drop to an overall loss of around 60% after 10,000 cycles.

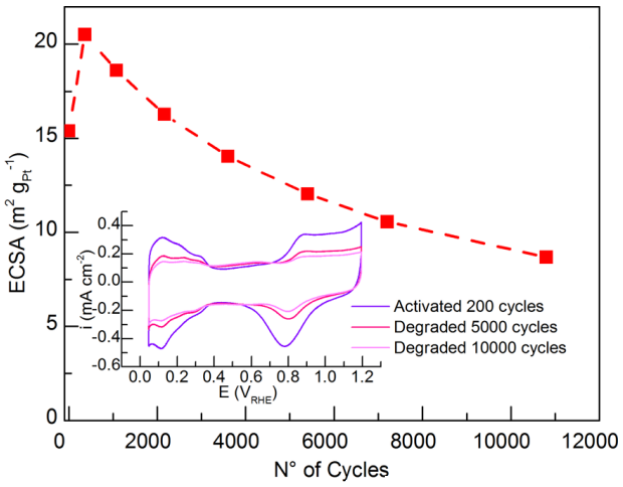

Figure 9. ECSA vs degradation cycles and representative CVs at defined intervals of the durability test (inset).[60]

In this series of catalysts, the dissolution of metals, including Pt and alloyed base metals, in electrochemistry operating condition could cause catalyst degradation. Also, the collapse of active catalyst nanostructure during fuel cell operation is also an issue. For example, the crystal facets that contain more catalytically active sites could be converted to a low active facet during the fuel cell processing.

1.4 Approaches for Nanostructured Pt Alloys

Commonly, "nanostructure" refers to a material with at least one dimension in the range of 1-100 nm.[38] In recent years, nanostructures with different shapes, including

particles, wires, rods, tubes and spheres, have been explored as electrocalalysts in the fuel cell.[59]

To date, many strategies have been developed for low cost, high activity and stability nanostructured Pt-alloy catalysts. The nanostructured Pt-alloy catalysts can be grouped into different clusters: (i) Pt-alloy nanoparticles, (ii) Pt-alloy nanotextures such as Pt-skins/monolayers, and (iii) branched or anisotropic elongated Pt or Pt-alloy nanostructures. Figure 10 presents the research trend in development of effective Pt-based nanostructure catalysts for ORR.[58]

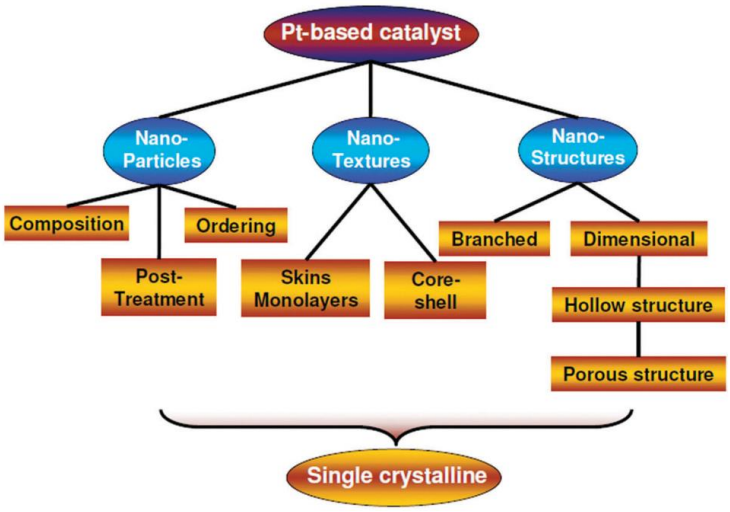

Figure 10. Schematic representation of the research trend in the development of effective Pt-based catalysts for PEM fuel cell applications.[58]

1.4.1 Two-dimensional (2D) Electrocatalysts

Two-dimensional (2D) materials are materials which exhibit similar and much stronger atomic organization and bond strength along two-dimensions compare with the third dimension. 2D materials have very high surface area, consisting of single or a few layers of atoms with quantum confined atomic and electronic structures.[96] Graphene is

one of the most commonly used 2D material in electrocatalysts, however, as mentioned above, the carbon corrosion issue hinders the stability of carbon supported catalysts.

1.4.2 2D Transition Metal Hydroxide Nanosheet

In addition to graphene, 2D metal hydroxides have been shown be able to be synthesized. So far, many methods to prepare nickel hydroxide materials have been reported.[110-112] Overall, α-$Ni(OH)_2$ can be prepared in bulk or as a micro-/nanoscale thin layer by chemical precipitation, electrochemical precipitation, sol-gel synthesis, hydrothermal or solvothermal.

$Ni(OH)_2$ may also be prepared by microwave-assisted synthesis.[35] It has been reported that microwave oven can heat a solution more homogeneously than conventional heating. It can produce uniform nanoparticle shapes and narrow size distributions. Figure 11 shows the morphology of α-nickel hydroxide synthesized by microwave.

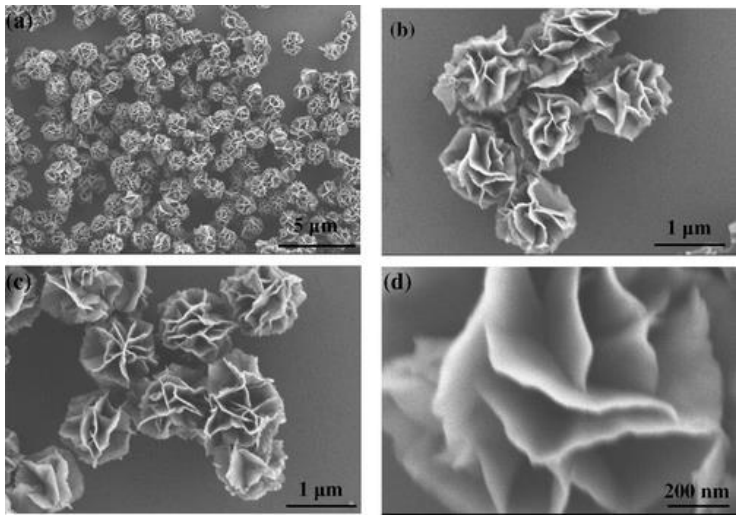

Figure 11. FE-SEM images of α-$Ni(OH)_2$ at different magnifications.[36]

For the solution-phase synthesis (either microwave or hydrothermal process), the reaction involves two steps: hydrolysis and condensation.[107] In aqueous solutions, Ni^{2+} form complexes, with the coordination number and type of coordinating ligand (either

OH_2 or OH^-) dependent on concentration and pH. Urea can be used as a slow release pH-adjusting agent to provide OH^- ions that coordinate with Ni^{2+}. At sufficiently high pH, the transition metal complex will under condensation reactions that form larger clusters/particles that precipitate as $Ni(OH)_2$.

Bode *et al*. first identified the two fundamental phases of nickel hydroxide, denoted as α-$Ni(OH)_2$ and β-$Ni(OH)_2$.[31] A sample XRD pattern is shown in Figure 12.

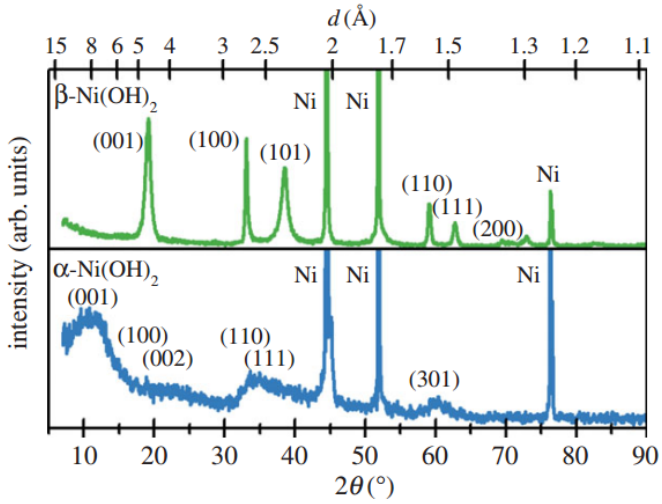

Figure 12. X-ray diffraction patterns of $Ni(OH)_2$ films on Ni substrates.

In Figure 13, the unit cell parameters for the stoichiometry ($3Ni:2H_2O$) are a = b = 5.335Å and c = 8.0Å.

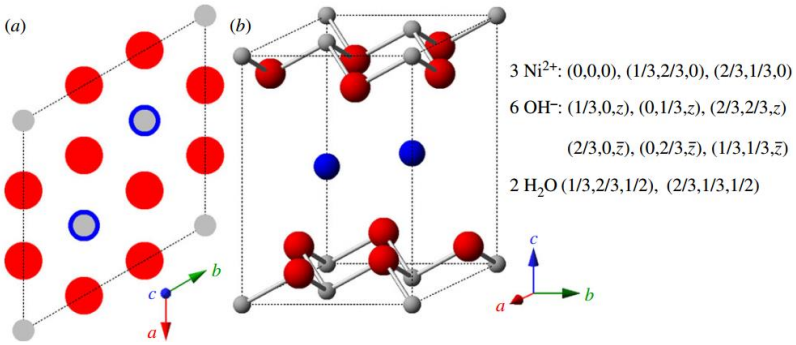

Figure 13. The idealized crystal structure of α-$Ni(OH)_2 \cdot xH_2O$ represented by (a) unit cell projection and (b) ball-and-stick unit cell for x=0.67 (actual value varies, $0.41 \leq x \leq 0.7$). Grey spheres, Ni^{2+}; red spheres, OH^-; blue spheres, H_2O.

There are several types of structural disorder, including the variable hydration, incorporation of foreign ions and crystal defects like stacking faults.[32] For α -$Ni(OH)_2$, TGA has shown that interlayer water may be removed at relatively high temperatures, T ≈ 240-300°C[33], and that it may occur together with the removal of water from the decomposition of the hydroxide to NiO.[34]

α-$Co(OH)_2$[62] and γ-CoOOH[64] nanosheets also have been prepared by a hydrothermal method. In Figure 14a, α-$Co(OH)_2$ nanosheet possesses a highly (001) preferred orientation. Figure 14b shows the α-$Co(OH)_2$ nanosheets are several hundred nanometers in size with the average thickness of only about 1.6 nm. Figure 14c shows the lattice parameter for α-$Co(OH)_2$. Commonly, the c direction is large (more than 7.0 Å) due to interlayer water, and the size of a-axis is 3.09 Å.[108] However, no prior work on microwork on microwave synthesis of $Co(OH)_2$ nanosheets has been reported.

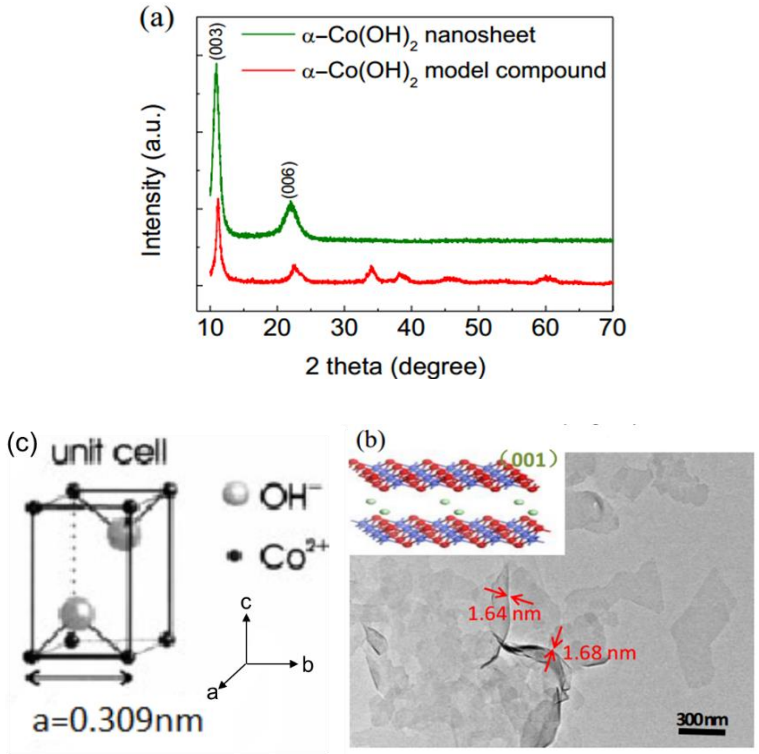

Figure. 14 (a) XRD pattern of synthesized α-$Co(OH)_2$ nanosheet and α-$Co(OH)_2$ model compound; (b) TEM image for α-$Co(OH)_2$ nanosheet; (c) Unit cell of α-$Co(OH)_2$

1.4.3 Ni-Pt 2D Nanoframes

Prior work showed that metallic Ni-Pt 2D nanoframes were synthesized by annealing of Pt-decorated $Ni(OH)_2$ nanosheets. [97] Ni-Pt 2D nanoframes are carbon-free electrocatalysts and exhibit significantly higher ORR catalytic activities and stabilities than Pt/C. The specific activity of the catalyst was determined to be 8 times higher than Pt/C and shows only 7% specific activity loss after 1000 cycles.

1.5 Motivation for the Current Work

The motivation of the project is to investigate the effect of cobalt on catalytic activity and long term stabiliy of unsupported (carbon free) metallic Pt-alloy catalyst toward ORR for PEMFCs. Pt has been shown to have higher activity when alloying with Co. Cobalt hydroxide nanosheets have large specific surface area which can provide a

good dispersion of the active component and good electric conductivity. Mild heat treatment in reduction condition can further increase the attachment between the support and the catalyst particles. At the same time, the temperature treatment will also cause strong electronic interaction between the support and the catalyst particles which can benefit the ORR kinetics. The three specific research objectives were as follows: i) synthesize Co-Pt 2D nanoframes and determine their structure and ORR activity; ii) determine the effect of thermal treatment temperature on the structure and activity of Co-Pt 2D nanoframes; iii) determine the effect of incorporation of Ni into Co-Pt 2D nanoframes (Co-Ni-Pt) on structure and activity. The overall goal was to develop a low-cost Pt-alloy catalyst with high activity and long term stability toward ORR for the fuel cell.

2. MATERIALS AND METHODS

2.1 Materials

Cobalt nitrate hexahydrate ($Co(NO_3)_2 \cdot 6H_2O$, 98 %), nickel nitrate hexahydrate ($Ni(NO_3)_2 \cdot 6H_2O$, 98 %) and urea (N_2COH_4, 99.3%) were purchased from Alfa Aesar. Ethylene glycol, isopropanol (HPLC grade), and ACS grade water (18 MΩ-cm) were obtained from VWR Analytical. Potassium hexachloroplatinate (K_2PtCl_6, 99.98%) was obtained from Sigma-Aldrich. All electrochemical measurements were carried out in 0.1 M $HClO_4$ diluted from 70% $HClO_4$ (Veritas Doubly Distilled) (0.000001% Cl^-). All reagents were used without further purification.

2.2 Pt-Transition Metals (M=Ni and/or Co) Alloy Synthesis

Synthesis of α-Co(OH)₂ nanosheets: The α-$Co(OH)_2$ nanosheets were synthesized using a microwave-assisted process modified from prior report hydrothermal synthesis of α-$Ni(OH)_2$ nanosheets.[35, 67] To prepare the α-$Co(OH)_2$ nanosheets, 1.05 g (3.60 mmol) of $Co(NO_3)_2.6H_2O$ was combined with 0.6486 g (10.80 mmol) of urea in 3 mL of ultrapure water (18 MΩ-cm) and 21 mL of ethylene glycol (EG). The solution was then transferred into a 35mL microwave vial. The reaction was conducted in a Discover SP Microwave reactor at 120 °C for 10 min (150 watts) with active stirring. The reaction was then allowed to cool to room temperature by venting the reaction chamber with air. The light purple powder was separated by centrifugation (3000 RPM, 3 min, Thermo, Sorvall ST16) and subsequently rinsed five times with water and two times with isopropanol. Then, the powder was dried at 60 °C overnight. The dried powder was notated as $Co(OH)_2$ nanosheets.

The $Co_xNi_{1-x}(OH)_2$ nanosheets were synthesized using the same process with 0.525g (1.80 mmol) of $Ni(NO_3)_2.6H_2O$ and 0.525 g (1.80 mmol) of $Co(NO_3)_2.6H_2O$. The dried powder is notated as $Co_xNi_{1-x}(OH)_2$ nanosheets.

Decorated $M(OH)_2$:Pt (M=Co and/or Ni) nanosheets: The $M(OH)_2$ nanosheets were decorated with Pt using a microwave-assisted process modified from a previously reported method.[68] To deposit Pt on the $M(OH)_2$ nanosheets, 0.062 g K_2PtCl_6, corresponding to 20 wt. % of metallic Pt vs $M(OH)_2$ was dissolved in 25 mL of ultrapure water (18 MΩ-cm) and then 0.1 g of the prepared $M(OH)_2$ was then added to the solution. The suspension was sonicated for 5 min then stirred for 10 min. The suspension was then transferred to a 35mL microwave vial. The reaction was conducted in a Discover SP Microwave synthesis system at 120 °C for 10 min (150 watts) with active stirring. The reaction was then allowed to cool down to room temperature by venting the reaction chamber with air. The powder was separated by centrifugation (3000 RPM, 5 min, Thermo, Sorvall ST16) and subsequently rinsed five times with water and two times with isopropanol. Then, the powder was dried at 60 °C overnight. The dried powder was notated as $Co(OH)_2$:Pt or $Co_xNi_{1-x}(OH)_2$:Pt nanosheets.

2D M-Pt (M=Ni and/or Co) alloy nanoframes: The decorated $Co(OH)_2$:Pt nanosheets were thermally treatment at 200 °C, 300 °C, or 400 °C with a ramp rate of 10 °C/min from room temperature for 20 minutes under 100 mL/min flowing Ar/H_2 (95/5 vol. %). The decorated $Co_xNi_{1-x}(OH)_2$: Pt nanosheets were thermally treatment at 200 °C in same conditon. The synthesized samples were notated as Co-Pt-200, Co-Pt-300, Co-Pt-400, and Ni-Co-Pt-200.

2.3 Structural and Physical Characterization

Powder X-Ray diffraction (XRD) was used to identify crystalline phases of the material. Measurements were conducted using a Bruker AXS D8 Advance Powder X-Ray diffractometer with a Cu Kα ($\lambda = 1.5406$ Å) radiation source, operating at 40 kV and 25 mA and a high-resolution 1D Linxeye XE detector. The scan range of 2Θ was $5° < 2\Theta < 85°$ with a 0.01° increment.

Scanning electron microscope (SEM) and Energy Dispersive X-ray Spectroscopy (EDS) elemental mapping were used to characterize the morphology and the element distribution within the material. SEM and EDS images were obtained using a Helios NanoLab 400 DualBeam Field Emission Scanning Electron Microscope. The sample was dispersed in isopropanol and coated on aluminum holder for the measurements.

Brunauer–Emmett–Teller (BET) surface areas and pore size distributions were obtained from nitrogen adsorption/desorption isotherms measured using a Micromeritics ASAP 2020 surface area and porosimetry analyzer. Samples were degassed at 120 °C for 16 h prior to characterization.

2.4 Rotating Disk Electrochemical Characterization

The electrochemical measurements were conducted at constant temperature (298 K) in 0.1 M $HClO_4$ solution (4.465mL of 70 wt % $HClO_4$ solution diluted with ultrapure water to 500mL). A three electrodes cell with a rotating disk electrode (RDE) was used for determination of electrode surface areas and for examination of electrocatalytic activities. The system setup consisted of an Autolab PGSTAT128N bi-potentiostat and rotation control (Pine Instruments). A Pt mesh was used as the counter electrode. A freshly prepared reversible hydrogen electrode (RHE) was used as the reference

electrode. The potential of RHE was confirmed by a commercial saturated silver/sliver chloride reference electrode (0.199 V_{NHE}).

The catalyst ink was prepared by mixing around 4 mg of the catalyst with 4 mL of ultra-pure water (18.2 MΩ), followed by sonicating in an ultrasonic bath (Fisher, 40 kHz) for 5 minutes maintaining the temperature around 25 °C. Then 15 µL catalyst ink was deposited onto a mirror polished glassy carbon electrode (0.196 cm^2) and dry it in the air. 15 µL of a stock solution consisting of 2 mL of isopropanol and 20 µL of 5 wt% Nafion solution (Sigma-Aldrich) was added on the surface of dried catalyst layer to bind them together.[69] The obtained catalyst thin layer was used as the working electrode. The same ink formulation was used for all catalysts.

Before measurement, the electrochemical cell was cleaned thoroughly of cationic, anionic, and organic impurities to obtain reproducible measurements. The follow method was used for cleaning the cell in this work. The cell was soaked within a mixture of H_2SO_4 and H_2O_2 (v:v =1:1) overnight. Then, the cell was rinsed with ultra-pure water 2 times and finally boiled at least 3 times with ultra-pure water.[69, 69]

The electrodes were immersed in 0.1 M $HClO_4$ under potential control at 0.1 V and then purged with Argon for 15min. The catalysts were conditioned by cycling 60 times between 0.05 and 1.2 V_{RHE} at a scan rate 100 mV s^{-1}, and 20 cycles between 0.05 and 1.2 V_{RHE} at a scan rate 20 mV s^{-1} with Argon-purging to produce a stable electrode surface. The hydrogen underpotential deposition (H_{upd}) charge over the H desorption region was integrated to obtained the Pt electrochemical surface area ($ECSA_{Pt\text{-}Hupd}$). The electrochemical surface area using CO stripping, $ECSA_{Pt,CO}$, was calculated by CO-

stripping obtained using a scan rate of 20 mV s^{-1}.[71] Equation 5 was used to calculate the $ECSA_{Pt}$.

$$ECSA_{Pt,cat}(m^2 g_{Pt}^{-1}) = \left[\frac{Q_{H-adsorption}(C) \text{ or } Q_{CO}/2(C)}{210 \mu C\, cm_{Pt}^{-2}\; L_{Pt}(mg_{Pt}\, m^{-2}) A_g(cm^2)}\right] 10^5 \qquad (5)$$

For evaluation of the oxygen reduction activity, IR-compensation and background subtraction were utilized for the measument.[70] Cyclic voltammetry was obtained from 0.05 to 1.1 V_{RHE} using a scan rate 20 mV s^{-1} and rotation rate of 1600 rpm in oxygen-saturated 0.1 M $HClO_4$. Prior of the ORR measurement, cyclic voltammograms were obtained under an Ar-purged electrolyte using the same parameters as used for the background. The ORR specific and mass activity are calculated by normalizing the kinetic current to the $ECSA_{Pt,\ Hupd}$ and the Pt loading on the electrode.[92] The $ECSA_{Pt}$ used for the calculation of the ORR specific activity was determined from the $ECSA_{Pt,Hupd}$ (equation 5).

3. RESULTS AND DISCUSSION

3.1 Overview of Synthesis Approach

The M (M=Co, Ni)-Pt alloy nanoframes were synthesized by three steps as summarized in Figure 15. The first step is formation of α-$M(OH)_2$ nanosheets using a microwave assisted process.[36] The nanosheets can provide a large surface for dispersion of Pt. The second step is the deposition of Pt on the surface of nanosheets using a similar microwave process. The third step is using controlled temperature/atmosphere treatments (H_2/Ar, 5/95 vol %) to transfer the Pt decorated α-$M(OH)_2$ nanosheets to a metallic phase and increase the interaction between the metal support and the Pt. 67

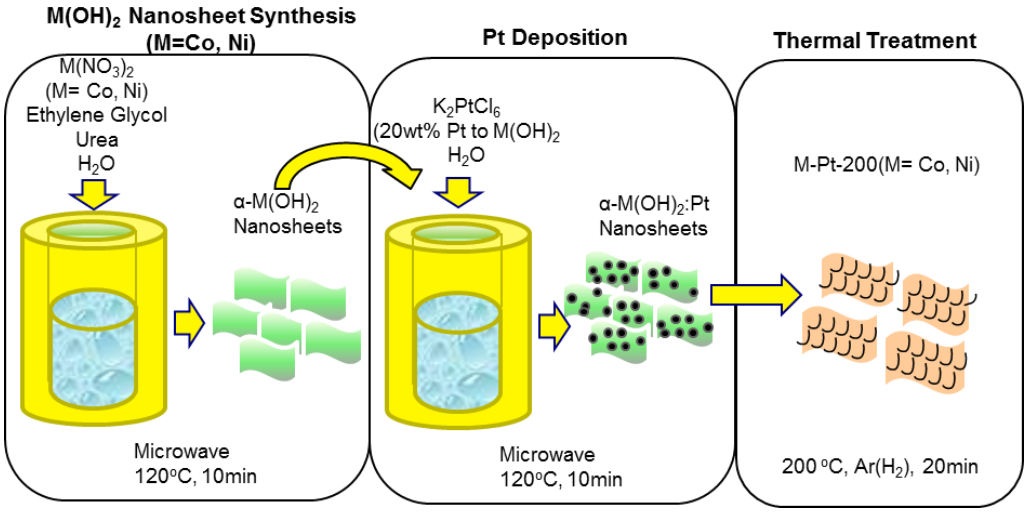

Figure 15. Schematic representation of the experimental steps for the synthesis of Metal-Pt alloy.

3.2 Binary Co-Pt Alloy Nanoframes Catalyst

3.2.1 Synthesis and Structure Characterization of Co-Pt 2D Nanoframes

The $Co(OH)_2$ nanosheets were synthesized by a solution-phase process using a microwave-assisted method adapted from $Ni(OH)_2$ nanosheets.[35] This method is based on the interaction of the aqueous Co^{2+} solution-phase species obtained from dissolving the

cobalt salt ($Co(NO_3)_2 \cdot 6H_2O$) with hydroxyl groups (generated from urea hydrolysis).[73] Hydrolysis of urea at elevated temperatures (120 °C) provides hydroxyl groups, and a small amount of water is added in in this reaction. The reactions involved in the formation of $Co(OH)_2$ are shown below:

$$NH_2\,CONH_2 \rightarrow NH_4^+ + NCO^- \quad (6)$$

$$NCO^- + 3H_2O \rightarrow HCO_3^- + NH_4^+ + OH^- \quad (7)$$

$$Co^{2+} + 2OH^- \rightarrow Co(OH)_2 \quad (8)$$

The solution-phase synthesis of $Co(OH)_2$ proceeds through hydrolysis and condensation reactions.[107]

The role of EG in this reaction includes four functions: firstly, the boiling point of EG is 197.3 °C, the high boiling point of EG is favorable for this reaction; secondly, EG is used as an intercalating agent extensively,[74, 75] so it may be incorporated into the $Co(OH)_2$ nanosheets layers. Thirdly, EG can affect the structures and morphology of the products. EG can act as a structure directing agent that coordinates with transition metal complexes as a chelating ligand. Fourthly, it may influence the kinetic of hydrolysis and condensation reactions. Thus, EG may control the composition, structure, and morphology of the products.[74, 76]

The SEM image of the as-prepared $Co(OH)_2$ is shown in Figure 16. The compound exists as a nanosheet structure. The lateral size of the nanosheets is ~1-2 μm. As shown in Figure 17 (a), the N_2 adsorption-desorption isotherm plot of $Co(OH)_2$ nanosheets exhibit the type II characteristic hysteresis loop which is consistent with meso-porosity within the $Co(OH)_2$. Figure 17 (b) shows the pore volume and size distribution of the mesopores. The $Co(OH)_2$ demonstrates pores that are conferred around

two pore sizes: 3 nm and 30 nm. The BET surface area of $Co(OH)_2$ was measured to be 78.4 m^2/g.

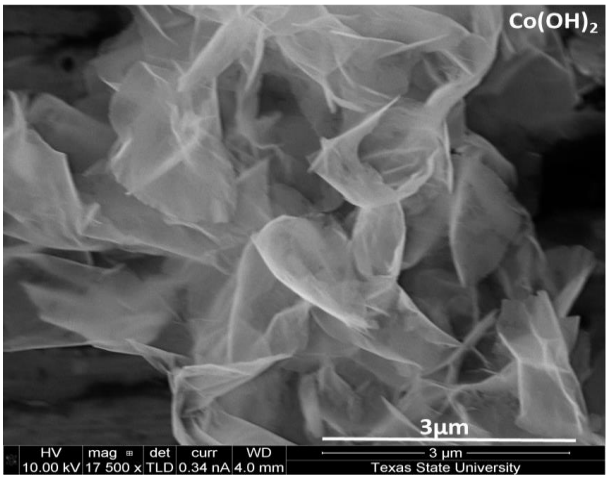

Figure 16. SEM image of as prepared $Co(OH)_2$ nanosheets.

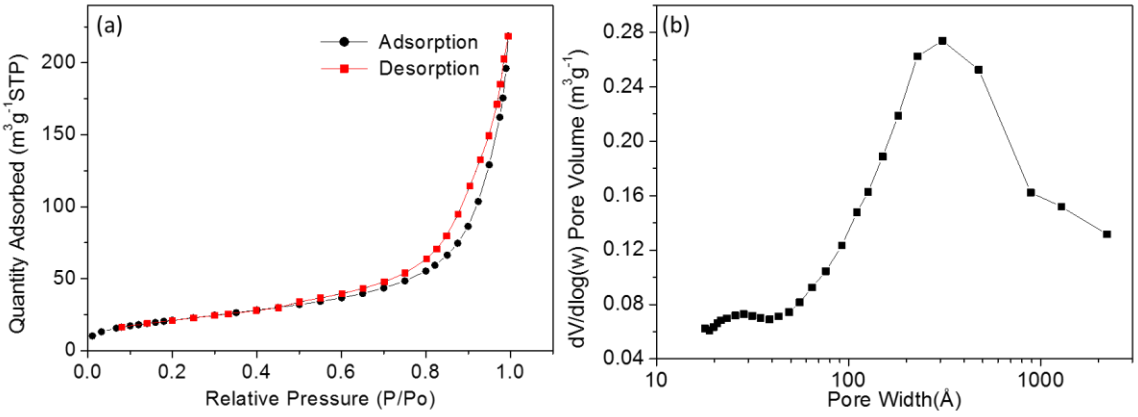

Figure 17. (a) Nitrogen sorption isotherms of $Co(OH)_2$ nanosheets; (b) Pore size distribution.

Electroless deposition of Pt is widely studied due to its significant practical importance in modern technologies. The deposition can be achieved by the incorporation of a reducing agent in the bath. So far, most widely used solutions for electroless deposition essentially contain hypophosphite, borohydride or alkylamine boranes as reducing

agents.[77] Furthermore, this redox reaction can proceed on catalytically active surfaces, such as metallic surfaces where the metal may be oxidized (act as a reducing agent). Kokkinidis *et al*. demonstrated that platinum can be deposited on metallic titanium surface at open-circuit potential in an aqueous 0.1 M $HClO_4$ solution containing K_2PtCl_6.[78] Diaz *et al*. reported that using $SnSO_4$ act as reducing agent in the electroless reduction of $(NH_4)_2PtCl_4$ that proceeds through an electronic exchange mechanism and can produce Pt-decorated SnO_2 powders.[109]

A microwave assisted process that avoids usage of any extra reducing agents was used. In this method, platinum can be deposited on $Co(OH)_2$ by immersing the metal hydroxide nanosheets into aqueous solution of K_2PtCl_6 and heating up to 120 °C. In this case, $Co(OH)_2$ may function as reducing agent and convert to CoOOH, however further investigation of the mechanism of Pt deposition onto $Co(OH)_2$ and the specific reducing agent of this reaction is needed.

As shown in Figure 18, the $Co(OH)_2$:Pt material maintains the nanosheet morphology of the $Co(OH)_2$ precursor. Some tiny white particles on the surface of $Co(OH)_2$ nanosheets were observed, suggests some Pt particles aggregates are present.

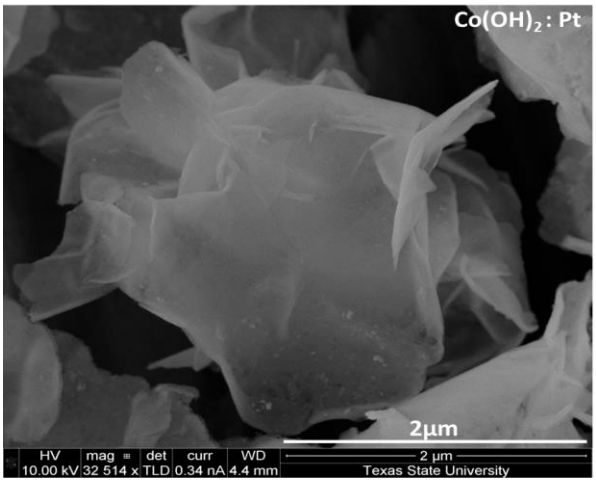

Figure 18. SEM image of $Co(OH)_2$ nanosheets deposited with Pt.

To promote direct Pt-Co interaction and transform the $Co(OH)_2$ phase into metallic Co ($Co(OH)_2 + H_2 \rightarrow Co + 2H_2O$), $Co(OH)_2$:Pt was heated under reducing conditions (H_2/Ar) at 200 °C. As observed from Figure 19 (a), after thermal treatment, Co-Pt-200 still exhibits a nanosheet morphology, however, the surface of the sample is not as smooth as before due to the formation of pores. Particularly, the heated samples no longer show the presence of Pt particles as within $Co(OH)_2$: Pt, which suggests Pt dispersed on the surface or within the material. Shown in Figure 19 (b-d) are EDS mapping images of the Co-Pt-200 shown that Co and Pt are homogeneously distributed on the catalyst. In addition, the presence of around 30% of oxygen indicates that the $Co(OH)_2$ may not completely transform to metallic Co, some oxide phases are present in the synthesized sample.[73]

The thermally treated samples exhibited a BET surface area of 31.2 m^2/g which is smaller than $Co(OH)_2$ nanosheets. The Co-Pt-200 shows a pores distribution around 60 nm which is larger than $Co(OH)_2$ (~30nm). The process of the $Co(OH)_2$ reduction maybe

accompanied by the formation of nuclei of metallic Co particles and the merging of the metallic particles which may lead to a reduced surface area[73, 79].

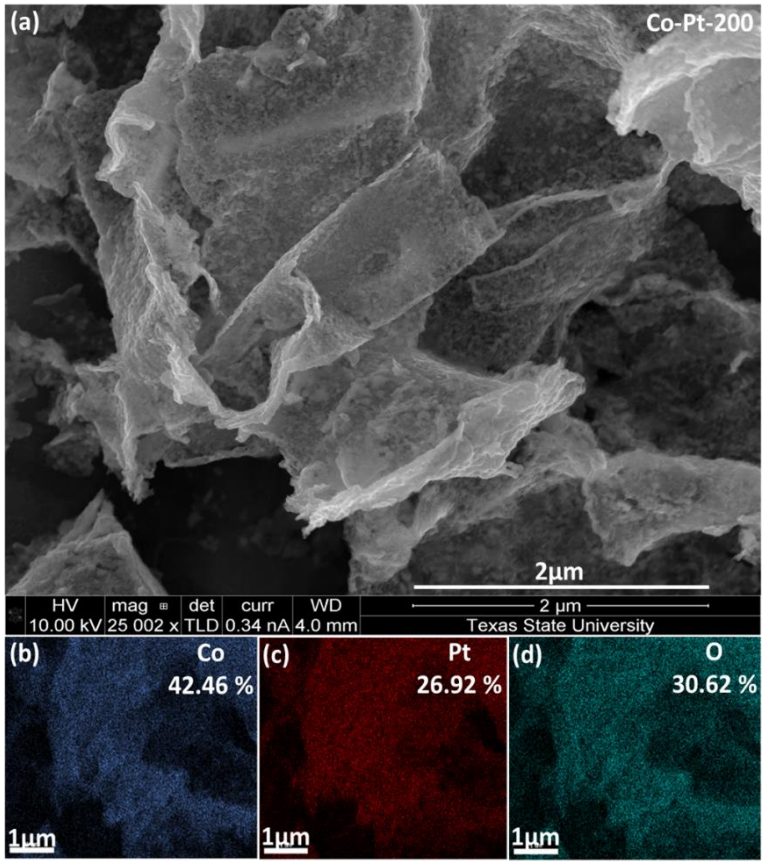

Figure 19. (a) SEM image of Co-Pt-200; (b-c) EDS elemental mapping.

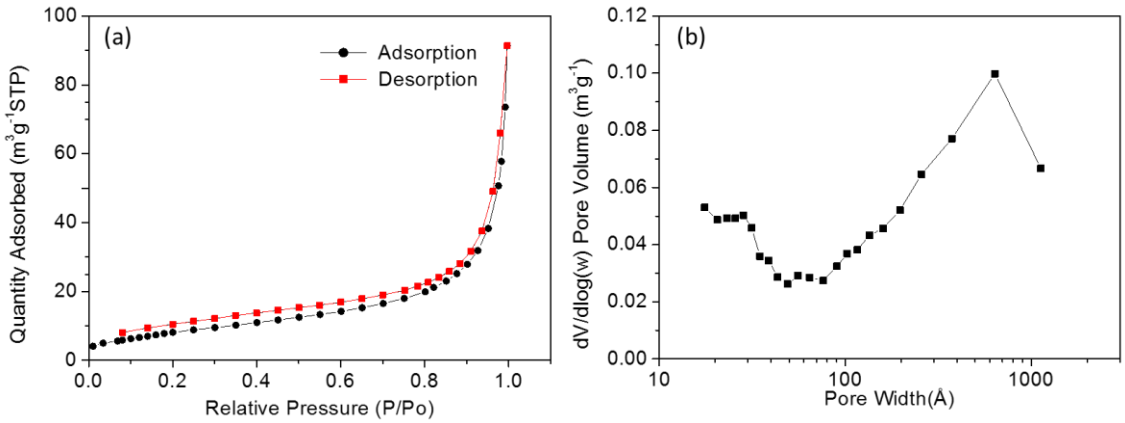

Figure 20. (a) Nitrogen sorption isotherms of Co-Pt-200; and (b) Pore size distribution

In Figure 21, XRD was used to characterize the synthesized materials and commercial Pt/C-Etek. The XRD pattern of the $Co(OH)_2$ nanosheets exhibit reflections at 2θ values of 12.1°, 24.4°, 32.8° and 58.0° which can be indexed as (001), (002), (100) and (110) crystal planes of α-$Co(OH)_2$ phase, respectively.[80, 81] The diffraction peak at 12.1° indexed to (001) plane of α-$Co(OH)_2$ is much stronger than the others which implies a significant degree of ordering of the (001) planes occurs within the α-$Co(OH)_2$ material. (001) and (002) are related to d-spacings that are multiples of each other due to multiple reflections from the basal plane.[82] The α-$Co(OH)_2$ exhibits a large interlayer spacing of 7.30 Å. It has been reported that the α-$Co(OH)_2$ synthesized using homogeneous precipitation methods from solution by hydrolysis of urea exhibits a sandwich-like structure. The formula is $Co(OH)_{1.85}(NH_3)_{0.4}(NO_3)_{0.15}$, which consists of positively charged $Co(OH)_{1.85}$ layers and charge balancing anions NO_3^- as well as ammonia and EG in the interlayer.[83, 84]

After Pt deposition, the powder XRD pattern of $Co(OH)_2$: Pt shows that the two peaks, (001) and (002), which belong to the basal planes are not present. There are no distinct peaks of due to Pt. Prior work of Pt deposition onto $Ni(OH)_2$ nanosheets has shown the presence of Pt.[97] However, the elemental mapping of the Co-Pt-200 demonstrated that Pt is present. Thus, the deposited Pt may have very poor crystallinity or even an amorphous structure. The new peak observed at 22.3° is in a similar range as cobalt oxyhydroxide (standard JCPDS card No. 01-073-1213) which has diffraction peak at 2θ=20.2° corresponding to the (003) plane.

After thermal treatment, significant structural modifications and phase changes were observed in the XRD patterns. The Co-Pt-200 sample did not present diffraction

peaks associated with α-$Co(OH)_2$. The sample shows the two main XRD peaks corresponding to Pt-fcc: (111) and (200). As shown in Table 2, the Pt (111) diffraction peaks of $2\theta=40.2°$ and Pt (200) of $2\theta=46.7°$ for Co-Pt-200 is slightly shifted to higher 2θ values when compared with the respective Pt peaks within commercial Pt/C-Etek (39.5° and 46.3°) which demonstrates that the Pt lattice distance was reduced by interaction with Co. It has been previously reported the smaller Pt-Pt interatomic distances in Pt alloys were due to the interaction of the alloying metal.[85] There were no distinct diffraction peaks observed that were consistent with a metallic Co phase. However, as observed in Figure 22, the sample developed magnetic properties which supports the presence of a metallic Co phase. Thus, the reduced Co may be highly disordered.

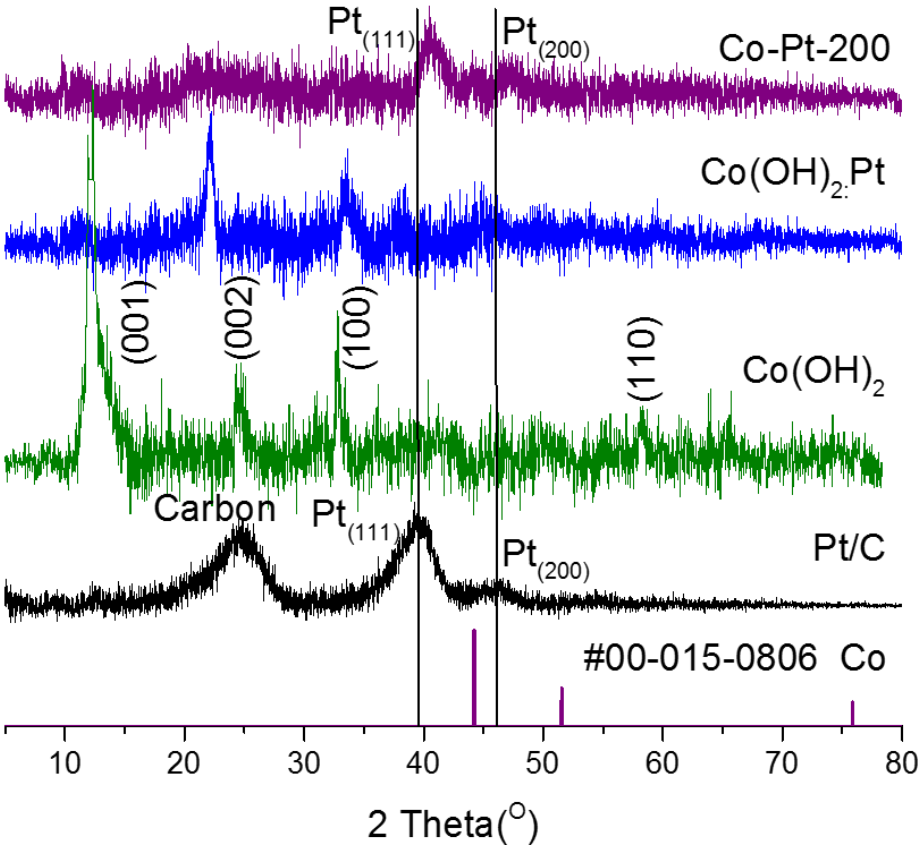

Figure 21. XRD of as-prepared $Co(OH)_2$, $Co(OH)_2$:Pt and their corresponding references: Co and Pt/C.

Table 2. Comparison of the lattice spacings of Pt in Pt/C and Co-Pt-200.

Sample ID	**Pt(2Θ)**	**Pt(Å) (111)**	**Pt(2Θ)**	**Pt(Å) (200)**
Pt/C	39.5	2.28	46.3	1.96
Co-Pt-200	40.2	2.24	46.7	1.94

Figure 22. Magnetic feature of Co-Pt-200.

3.2.2 Electrochemical Surface Area and Oxygen Reduction Reaction Activity of Co-Pt-200

CVs in N_2-saturated 0.1 M $HClO_4$ solution were obtained to determine the $ECSA_{Pt}$ of Co-Pt-200. Before measurement, catalysts were processed with an electrochemical activation step (60 scans between 0.05 and 1.2 V_{RHE} at a scan rate 100 mV s^{-1} and 20 scans between 0.05 and 1.2 V_{RHE} at a scan rate 20 mV s^{-1}). Figure 23 shows the H_{upd} region in first cycle of conditioning of Co-Pt-200 and shows that Co-Pt-200 doesn't initially exhibit polycrystalline platinum profiles which suggests that the clean Pt is not accessible on the surface of catalyst at the beginning. However, after a few cycles, polycrystalline platinum profiles are observed which may be due to removal of metallic Co and oxide phases from the surface.

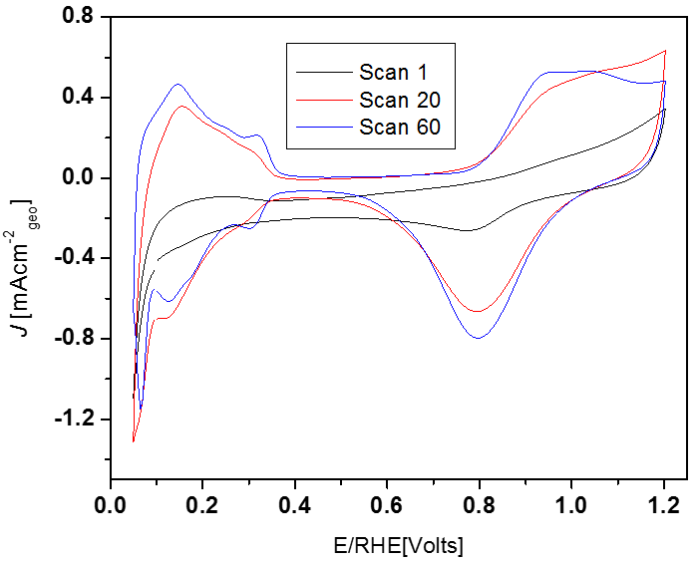

Figure 23. Cyclic voltammetry of Co-Pt-200 during electrochemical conditioning at the 1st, 20th and 40th cycle.

Figure 24(a) shows the CV curves of Pt/C and Co-Pt-200 after the activation step. The voltammograms showed polycrystalline platinum profiles similar with that of the Pt/C. The current density was normalized to the geometric surface area of the electrode. The H_{upd} peaks appear at E < 0.4 V and Pt oxidation and reduction peaks at 0.9 and 0.8 V in the anodic and cathodic scans, respectively. Compared with Pt/C, the Pt oxidation and reduction peaks of Co-Pt-200 catalysts have positive shifts of ~35 mV which is consistent with the trend of altered electronic structures of these alloys. This positive shift has been generally correlated with improved ORR activity.[16]

Figure 24(b) shows the electrochemical CO oxidation (CO stripping: $2CO + O_2 = 2CO_2$) curves of Pt/C and Co-Pt-200 between 0.6 and 1.0 V_{RHE} after subtraction of the second scan. The current density was normalized to the geometric surface area of the electrode. CO stripping is a surface sensitive reaction which depends on surface conformation, composition, particle size and shape, thus, it has been used to

characterize the catalyst surface.[86] In this reaction, the electrolyte is first saturated with a CO for 25min. The electrode is adhered with a CO layer at $0.1V_{RHE}$. Owing to a strong Pt-CO_{ad} interaction, CO molecules stay adsorbed on Pt surface. Then, the electrolyte is purged with Ar gas for 25min. The following step involves electro-oxidation of CO by sweeping the potential towards the positive limit.[86] The Co-Pt-200 catalyst displays a predominantly single CO stripping peak at a lower potential (0.68 V) compared with commercial Pt/C (0.79 V) while the shape of the stripping peak is much broader than Pt/C. The lower onset potential for CO oxidation on Pt is attributed to weaker CO binding on Pt interacting with Co caused by the modified electronic properties as supported by density functional theory calculations.[87]

The $ECSA_{Pt,\ Hupd}$ of the catalysts was obtained by calculating the charge using the hydrogen under potential desorption (H_{upd}) area.[88] As shown in Table 3, the calculated $ECSA_{Pt,\ Hupd}$ of Co-Pt-200 is 24.9 $m^2g^{-1}_{Pt}$ which is lower than the Pt/C catalyst (72.1 $m^2g^{-1}_{Pt}$). The Pt electrochemical surface area ($ECSA_{Pt,\ CO}$) of Co-Pt-200 calculated by the CO-stripping peak integration is 23.4 $m^2g^{-1}_{Pt}$. Moreover, the ratio between the charges of CO stripping versus H_{upd} is calculated to character the difference in adsorption properties of catalyst surface. The experimental $Q_{CO}/2Q_H$ ratio of Co-Pt-200 is 0.94 which is consistent with a Pt-skeleton arrangement ($Q_{CO}/2Q_H \sim 1$)[89] rather that a Pt-skin which showed a $Q_{CO}/2Q_H$ ratio of ~ 1.5.[86]

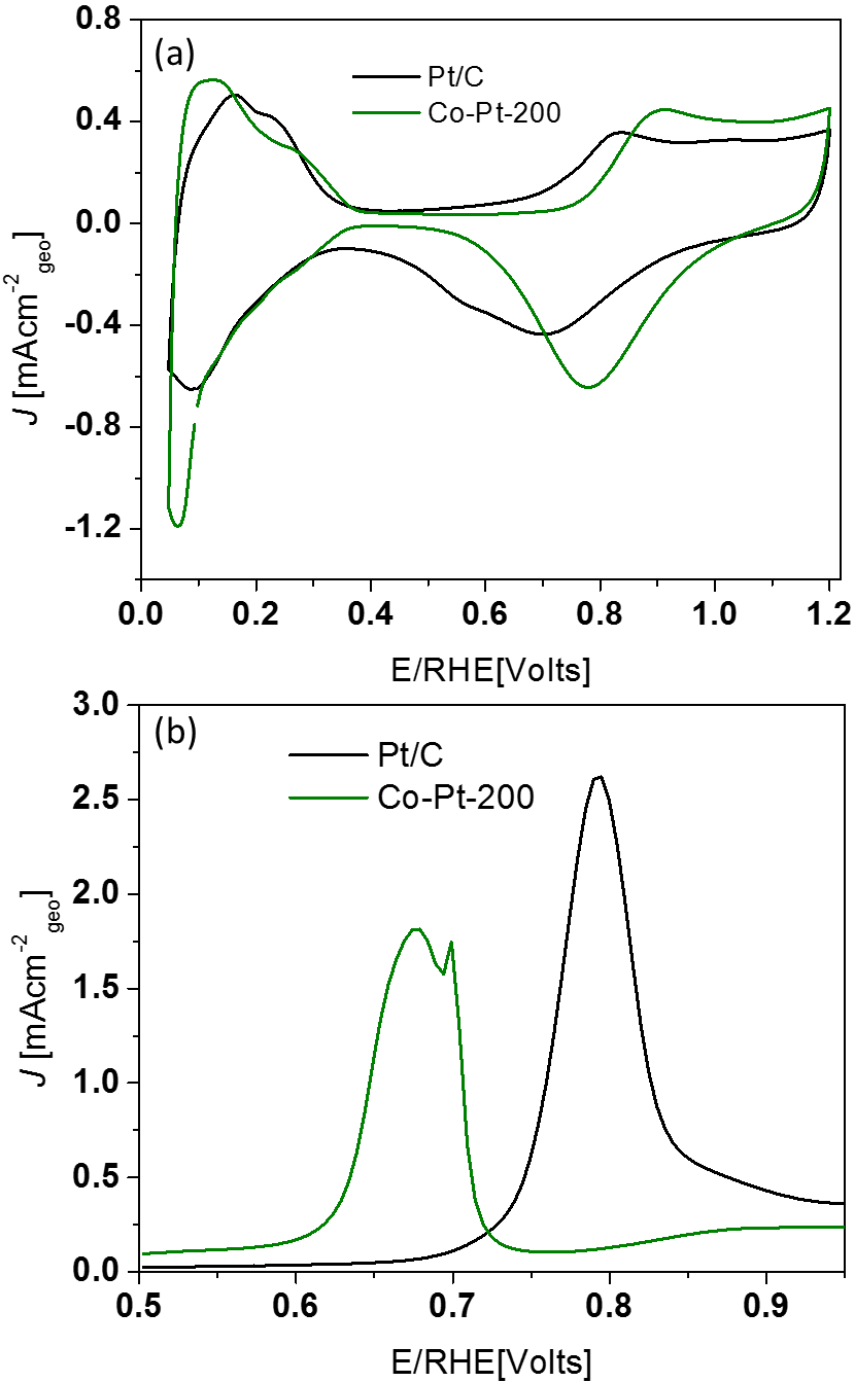

Figure 24. Electrochemistry of Co-Pt-200 and commercial Pt/C; (a) cyclic voltammetry (electrolyte 0.1 M $HClO_4$ Ar-saturated, scan rate: 20 mV s^{-1}); (b) carbon monoxide (CO) stripping voltammetry. Platinum loadings were L_{Pt}= 26.3 µg cm^{-2}_{geo} (Pt/C) and 25 µg cm^{-2}_{geo} (Co-Pt-200).

Table 3. Comparison of the platinum electrochemical surface area ($ECSA_{Pt}$) from CO stripping ($ECSA_{Pt,CO}$) and H_{upd} regions ($ECSA_{Pt,Hupd}$) and the ratio of $ECSA_{Pt}$ from CO stripping and H_{upd} regions of Pt/C and Co-Pt-200.

Sample ID	**$ECSA_{Pt, CO}$ ($m^2\ g^{-1}_{Pt}$)**	**$ECSA_{Pt, Hupd}$ ($m^2\ g^{-1}_{Pt}$)**	**Ratio $ECSA_{Pt, CO}$ / $ECSA_{Pt, Hupd}$ ($Q_{CO}/2Q_H$)**
Pt/C	75.4	72.1	1.04
Co-Pt-200	23.4	24.9	0.94

Figure 25(a) shows the hydrodynamic polarization curves of Pt/C and Co-Pt-200 in an O_2-saturated 0.1 M $HClO_4$ solution at a scan rate of 0.02 V/s, using a RDE at 1600 rpm. The current density was normalized to the geometric surface area of the electrode. The polarization curve exhibits two different potential regions: (i) a mixed kinetic-diffusion controlled region between 1.0 and 0.7 V_{RHE}; (ii) a diffusion limited plateau below ~0.7 V_{RHE}.[91] As discussed extensively by Mayrhofer *et al.*, the ORR current at the 0.9 V_{RHE} is typically used to obtain the activity toward ORR.**Error! Reference source not found.** C o-Pt-200 shows better catalytic activity toward the ORR than the Pt/C catalyst.

As shown in Figure 25(b-c), the Co-Pt-200 shows a specific activity at 0.9 V_{RHE} of 4.8 mA cm^{-2}_{Pt}. The specific activity of Co-Pt-300 is 8 times higher than the specific activity of Pt/C. In addition, the mass activity is 1.2 A mg^{-1}_{Pt} which is higher than the mass activity of Pt/C.

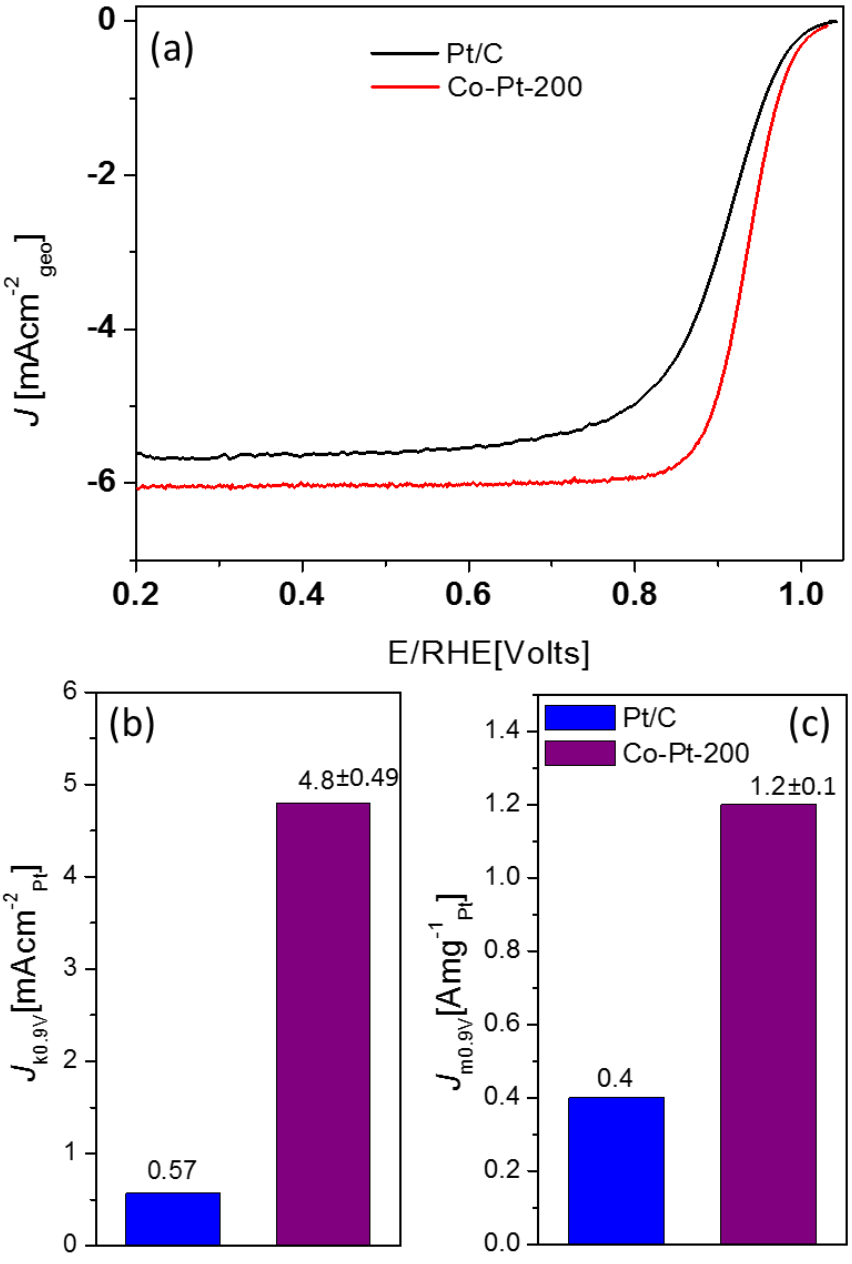

Figure 25. Electrochemistry of Co-Pt-200 and commercial Pt/C; (a) Potentiodynamic scans in ORR region (electrolyte 0.1 M $HClO_4$ O_2-saturated, scan rate: 20 mV s^{-1}, 1600 rpm); (b) comparison of ORR specific activities and (c) mass-normalized activities at 0.9 V_{RHE}. Platinum loadings were L_{Pt}= 26.3 µg cm^{-2}_{geo} (Pt/C) and 25 µg cm^{-2}_{geo} (Co-Pt-200).

3.3 The Effect of Thermal Treatment Temperature on Structure and Activity of Co-Pt Alloys

3.3.1 Structural and Physical Characterization of Co-Pt Alloys Treated in 300°C and 400°C

Higher thermal treatments were conducted to determine if higher temperatures could be used to remove oxygen and obtain a Co-Pt alloy phase. It was expected that too high temperatures would result in reduced porosity and lower activity. In Figure 26(a) and Figure 27(a), after the thermal treatment with higher temperatures (300°C and 400°C) under H_2/Ar, Co-Pt-300 and Co-Pt-400 exhibit a 2D nanoframe architecture with an interconnected network of solid and pores which is different from the nanosheet morphology of Co-Pt-200. The size of pores and solid particles was observed to be increased and may be due to higher temperature that can facilitate growth of particles. In Figure 26 (b-d) and Figure 27 (b-d), EDS mapping images of the Co-Pt-300 and Co-Pt-400 show that Co and Pt are homogeneously distributed on the catalysts. In addition, the percentage of oxygen element is also decreased indicating that the $Co(OH)_2$ and some oxide phase are further transformed to a metallic phase.

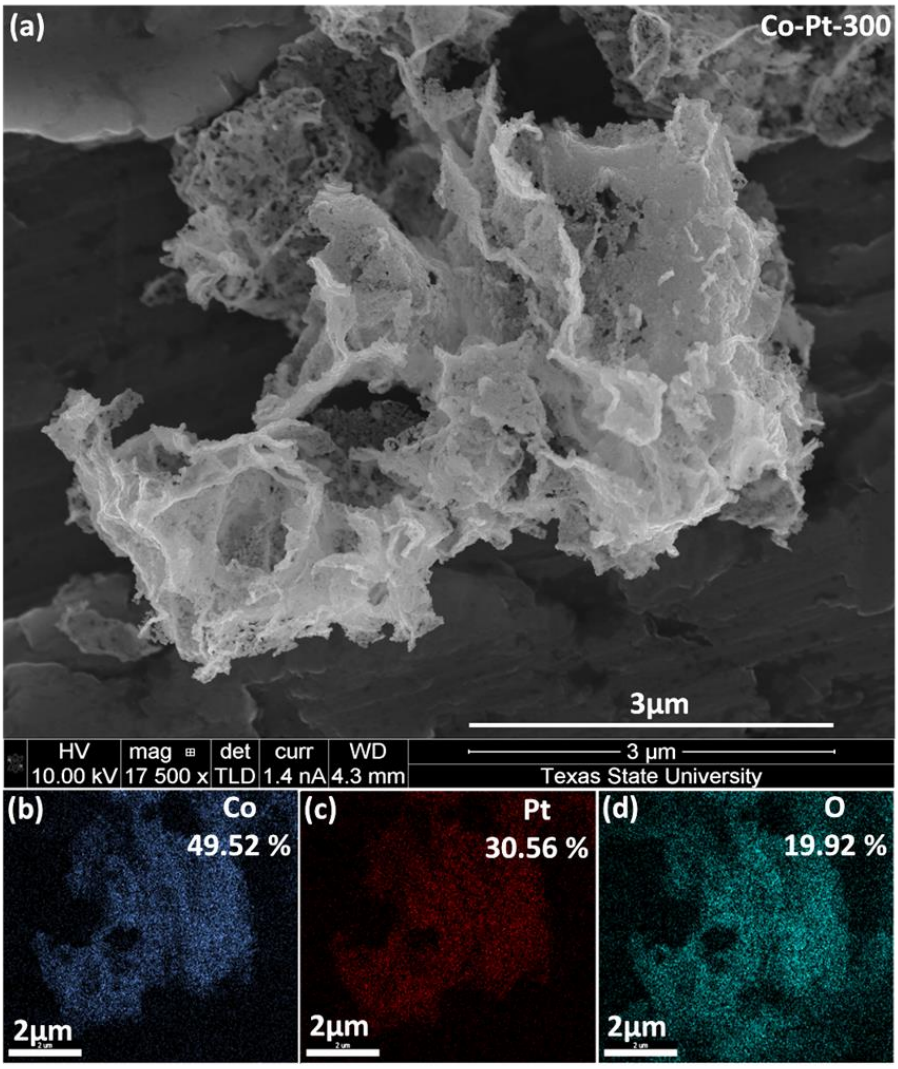

Figure 26. (a) SEM image of Co-Pt-300; (b-c) EDS elemental mapping.

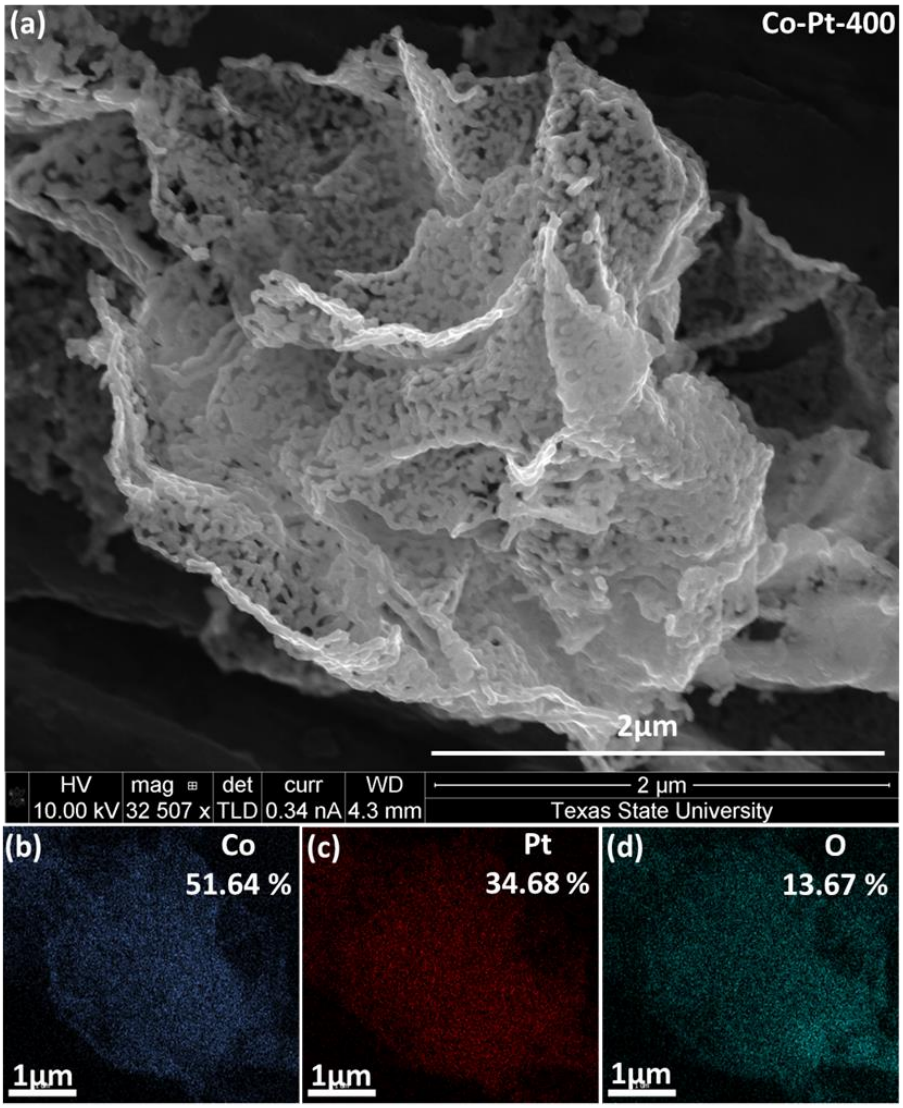

Figure 27. (a) SEM image of Co-Pt-400; (b-c) EDS elemental mapping.

As shown in Figure 28(a) and (c), both of adsorption-desorption isotherms plot of Co-Pt-300 and Co-Pt-400 exhibit the type II characteristic hysteresis loop which consistent with the presence of mesopores. Figure 28(b) and (d) show the pore volume and size distribution of catalyst. The Co-Pt-300 demonstrates a peak in pore volume around 60 nm. However, the Co-Pt-400 do not exhibit significantly peak for any pore

volume. The thermally treated samples exhibited BET surface areas of 32 and 14 m^2g^{-1} for the Co-Pt-300 and Co-Pt-400 respectively.

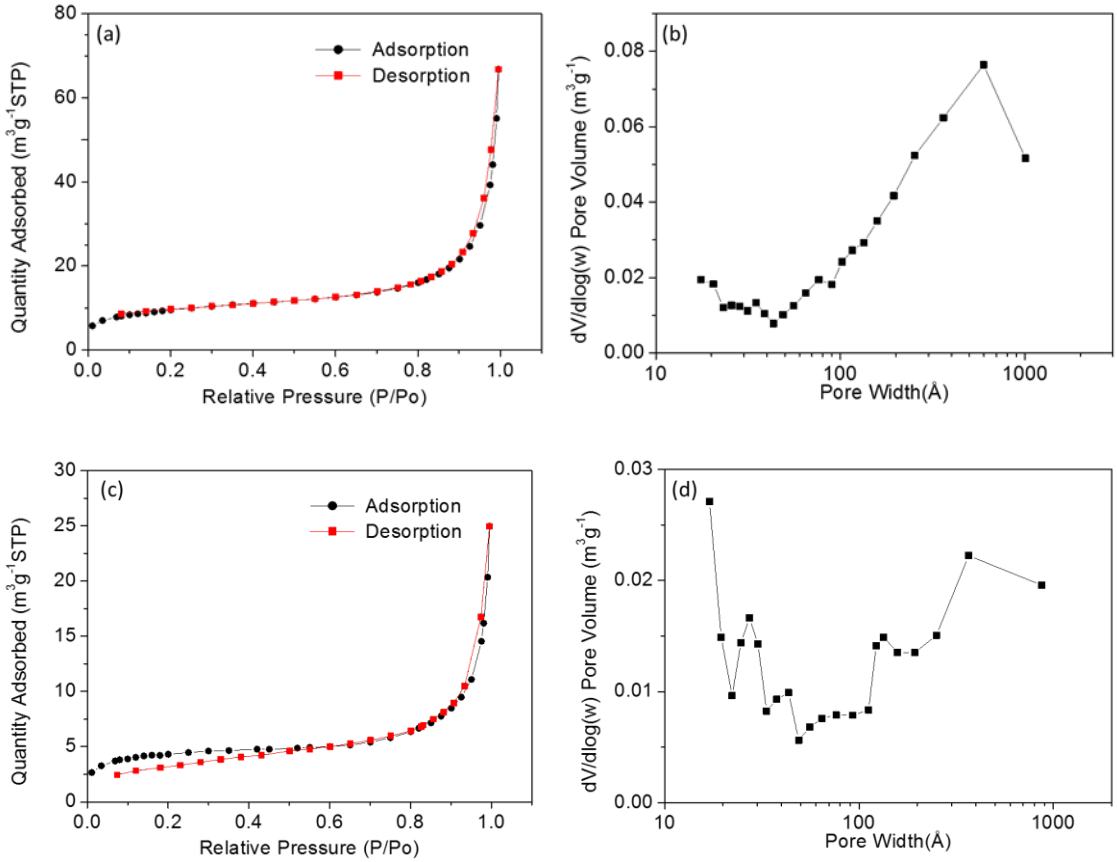

Figure 28. (a) Nitrogen sorption isotherms and (b) Pore size distribution of Co-Pt-300; (c) Nitrogen sorption isotherms and (d) Pore size distribution of Co-Pt-400.

As shown in Figure 29, after thermal treatment at higher temperatures, there were no new peaks in the XRD patterns. Co-Pt-200 shows the two main XRD peaks corresponding to Pt-fcc for (111) and (200). However, the main XRD peak in Co-Pt-300 and Co-Pt-400 shifts to higher 2θ values compared with the main peak within Co-Pt-200. The peak position of the main XRD peak is closer metallic Co than Pt, however, the 2Θ value is lower than within metallic Co which suggests a Co-Pt alloy is formed. In

addition, the narrower peak width for Co-Pt-400 is also consistent with a larger particle size. As shown in Figure 30, the sample developed magnetic properties which supports the presence of a metallic Co phase.

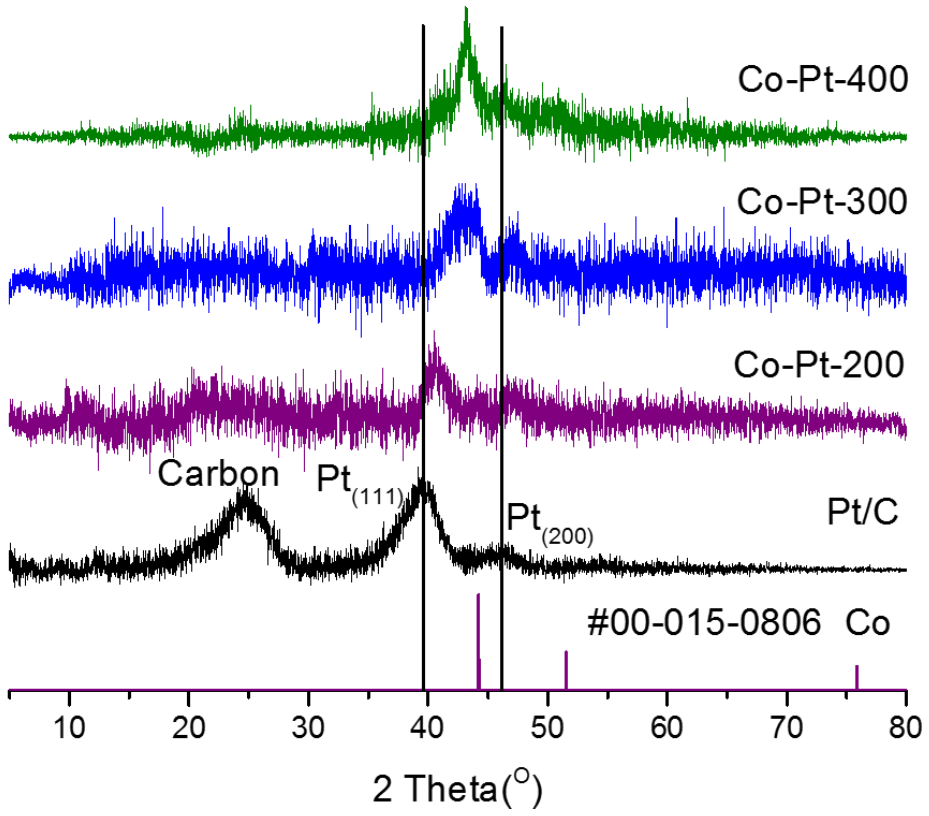

Figure 29. XRD of as-prepared catalysts at different temperatures and corresponding references: Co and Pt/C.

Figure 30. Magnetic feature of Co-Pt-300 and Co-Pt-400.

3.3.2 Electrochemical Surface Area and Oxygen Reduction Reaction Activity of Co-Pt alloys after Thermal Treatment

Figure 31(a) shows the CV curves of Co-Pt-200, Co-Pt-300, Co-Pt-400 and Pt/C in N_2-saturated 0.1 M $HClO_4$ solution. After the electrochemical activation, the voltammograms showed polycrystalline platinum profiles similar with that of the Pt/C. However, the features in the hydrogen adsorption/desorption region, and the Pt oxidation/reduction peaks still show subtle differences depending on the treatment temperature. As the temperature increased, the Pt oxidation and reduction peaks of catalysts have positive shifts gradually which is associated with the altered electronic structures of these alloys.[16] The higher temperature treated samples showed significant difference peak features at hydrogen desorption region, which are associated with different Pt nanocrystal facets.[93] The changes in the CV may reflect the changes in the particle sizes, structure and electronic properties of the catalysts.

Figure 31(b) shows the electrochemical CO oxidation (CO stripping) curves of catalysts with different temperature treatment and Pt/C between 0.6 and 1.0 V_{RHE} after

subtraction of the second scan. The thermal treatment catalysts display CO stripping peaks at lower potentials (0.68-0.70V) compared with commercial Pt/C (0.79 V). The lower onset potential for CO oxidation on Pt is attributed to weaker CO binding on Pt interacting with Co caused by the modified electronic properties based on density functional theory calculations.[87] Compared with the Co-Pt-200 catalyst, the Co-Pt-300 and Co-Pt-400 catalysts showed higher voltages for CO stripping, and the Co-Pt-200 sample showed the lowest voltage for CO stripping which corresponds to the weakest CO binding energy.

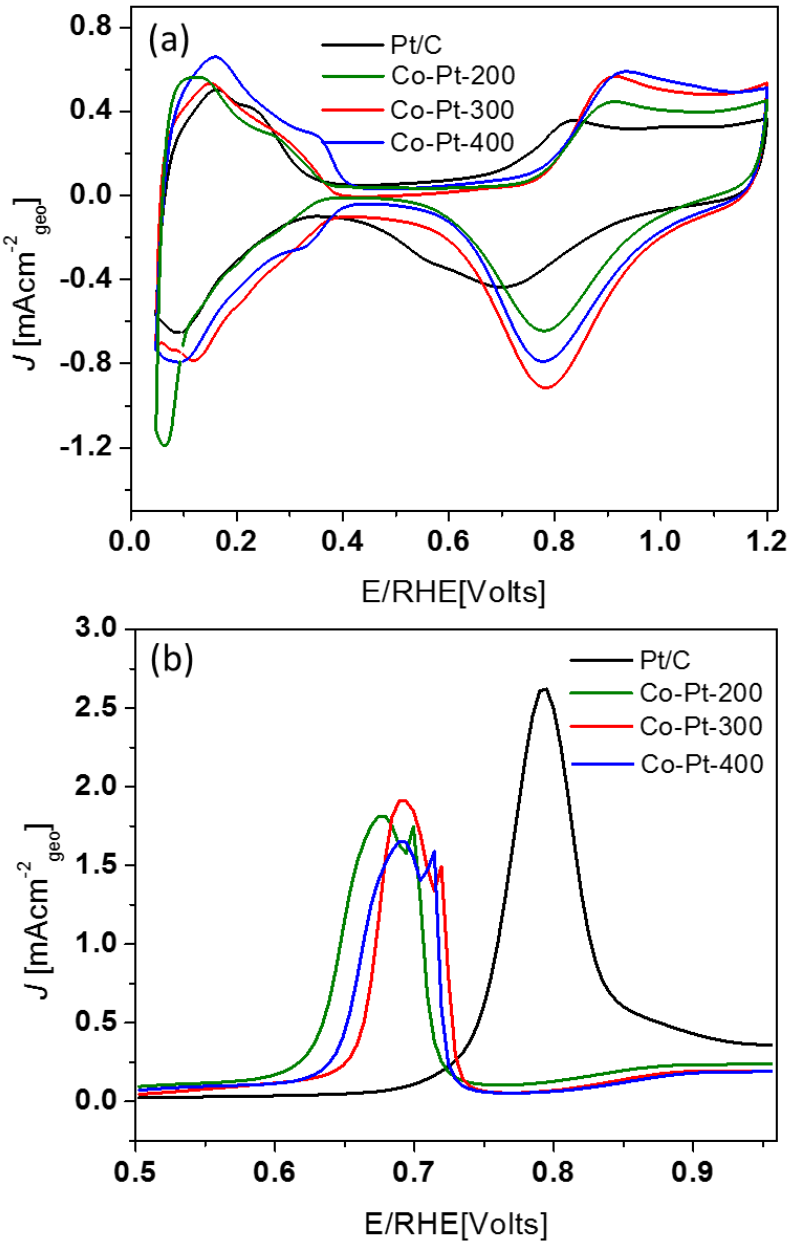

Figure 31. Electrochemistry of Co-Pt-200, Co-Pt-300, Co-Pt-400 and commercial Pt/C; (a) cyclic voltammetry (electrolyte 0.1 M $HClO_4$ Ar-saturated, scan rate: 20 mV s^{-1}); (b) carbon monoxide (CO) stripping voltammetry. Platinum loadings were L_{Pt}= 26.3 µg cm^{-2}_{geo} (Pt/C), 25 µg cm^{-2}_{geo} (Co-Pt-200), 26.8 µg cm^{-2}_{geo} (Co-Pt-300) and 30 µgcm^{-2}_{geo} (Co-Pt-400).

As shown in Table 4, the calculated $ECSA_{Pt, Hupd}$ and $ECSA_{Pt, CO}$ of catalysts with different temperature treatment are in a similar range. The ratio between the charges of CO stripping versus H_{upd} is calculated to character the difference in adsorption properties of catalyst surface. The experimental $Q_{CO}/2Q_H$ ratio of the thermal treatment catalysts are around 1 which is consistent with a Pt-skeleton arrangement ($Q_{CO}/2Q_H = 1$)[89] rather that a Pt-skin which showed a $Q_{CO}/2Q_H$ ratio of 1.5.[86]

Table 4. Comparison of the platinum electrochemical surface area ($ECSA_{Pt}$) from CO stripping ($ECSA_{Pt,CO}$) and H_{upd} regions ($ECSA_{Pt,Hupd}$) and the ratio of $ECSA_{Pt}$ from CO stripping and H_{upd} regions of Pt/C, Co-Pt-200, Co-Pt-300 and Co-Pt-200.

Catalyst	**$ECSA_{Pt, CO}$ ($m^2 g^{-1}Pt$)**	**$ECSA_{Pt, Hupd}$ ($m^2 g^{-1}Pt$)**	**Ratio $ECSA_{Pt, CO}$ / $ECSA_{Pt, Hupd}$ ($Q_{CO}/2Q_H$)**
Pt/C	75.4	72.1	1.04
Co-Pt-200	23.4	24.9	0.94
Co-Pt-300	23.5	21.3	1.10
Co-Pt-400	22.2	20.7	1.07

Figure 32(a) shows the hydrodynamic polarization curves of catalysts treated at 200°C, 300°C, 400°C and Pt/C. In the kinetic region of the hydrodynamic polarization curves at 0.9 V, the kinetic current increase with increasing treatment temperature. In Figure 32(b-c), the differences in the ORR specific activities between Co-Pt-200 and Co-Pt-300 were within experiment error. However, Co-Pt-400 showed a lower specific activity compared with Co-Pt-200. The mass activities of Co-Pt-300 and Co-Pt-400 were lower than Co-Pt-200.

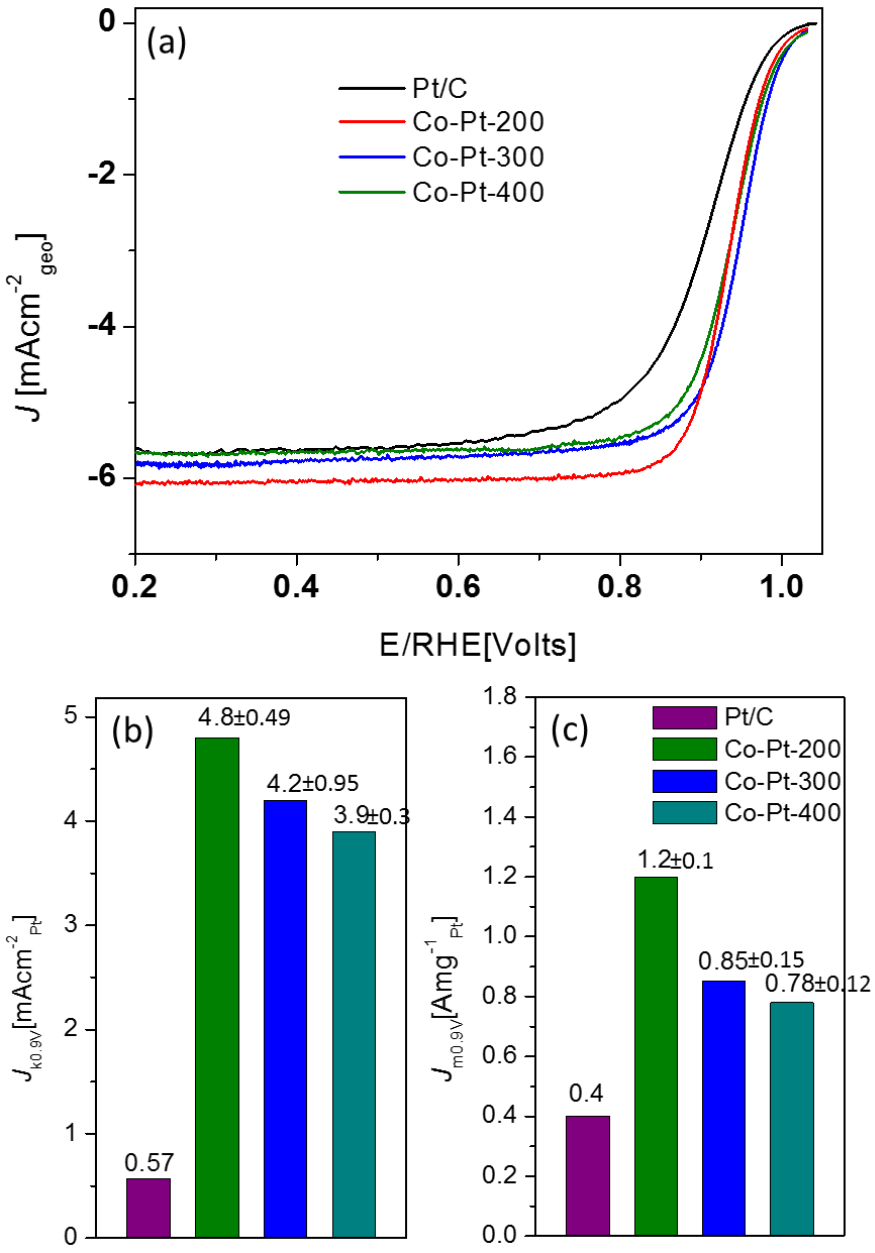

Figure 32. Electrochemistry of Co-Pt-200, Co-Pt-300, Co-Pt-400 and commercial Pt/C; (a) Potentiodynamic scans in ORR region (electrolyte 0.1 M $HClO_4$ O_2-saturated, scan rate: 20 mV s^{-1}, 1600 rpm); (b) comparison of ORR specific activities and (c) mass-normalized activities at 0.9 V_{RHE}. Platinum loadings were L_{Pt}= 26.3 µg cm^{-2}_{geo} (Pt/C), 25 µg cm^{-2}_{geo} (Co-Pt-200), 26.8 µg cm^{-2}_{geo} (Co-Pt-300) and 30 µg cm^{-2}_{geo} (Co-Pt-400).

3.4 The Effect of Incorporation Ni on Structure and Activity of Co-Pt Alloy

3.4.1 Structural and Physical Characterization of Ternary Co-Ni-Pt Alloy

The incorporation of Ni was also investigated. Base on prior work, adding third transitional metal into binary Pt-alloy can further increase the activity of catalyst.[66] The SEM image of the as prepared $Co_xNi_{1-x}(OH)_2$ is shown in Figure 33(a). The material exhibited a nanosheets structure with a flower shape. In figure 33 (b-d), EDS mapping images of the $Co_xNi_{1-x}(OH)_2$ showed that Co, Ni and O are homogeneously distributed on the catalyst. In addition, the ratio of Co and Ni is different from nominal ratio (1:1), suggesting the different reaction rate of hydrolysis and condensation between different metals.

As shown in Figure 34 (a), the adsorption-desorption isotherms plot of $Co_xNi_{1-x}(OH)_2$ nanosheets exhibit a type II characteristic hysteresis loop which consistent with the present of mesopores. Figure 34(b) shows the pore volume and size distribution of the catalysts. The $Co_xNi_{1-x}(OH)_2$ exhibits two peaks in pore volume with a peak around 4.5nm and 80 nm. The BET surface area of $Co_xNi_{1-x}(OH)_2$ is 99.6 m^2/g.

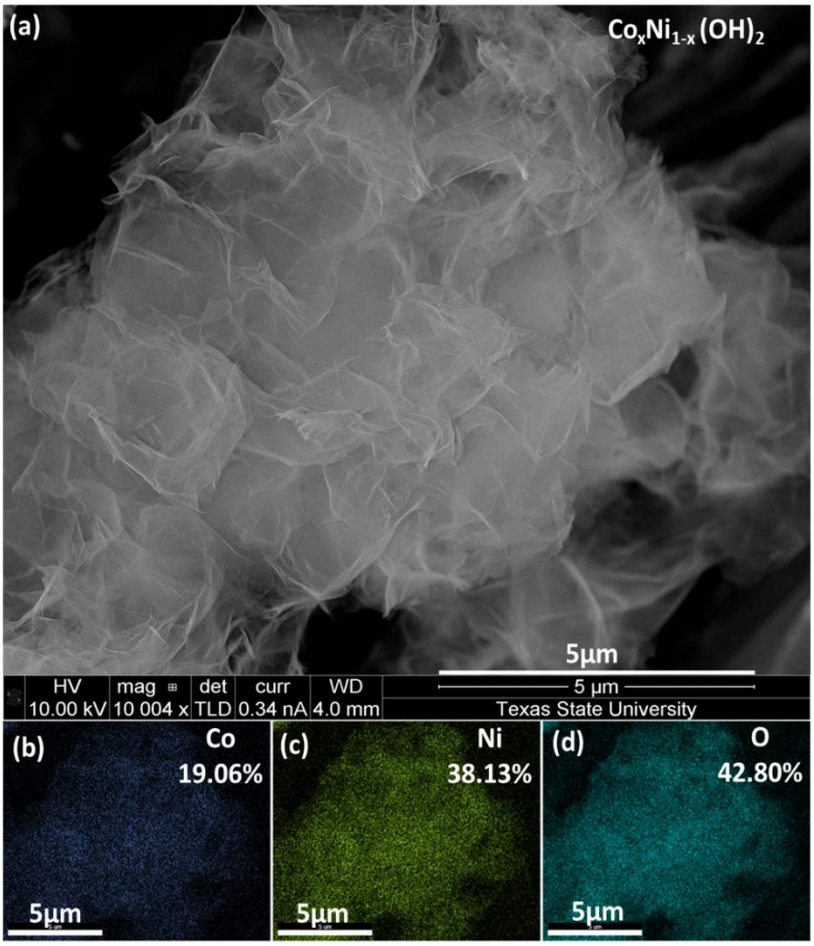

Figure 33. (a) SEM image of as prepared $Co_xNi_{1-x}(OH)_2$ nanosheets; (b-c) EDS elemental mapping.

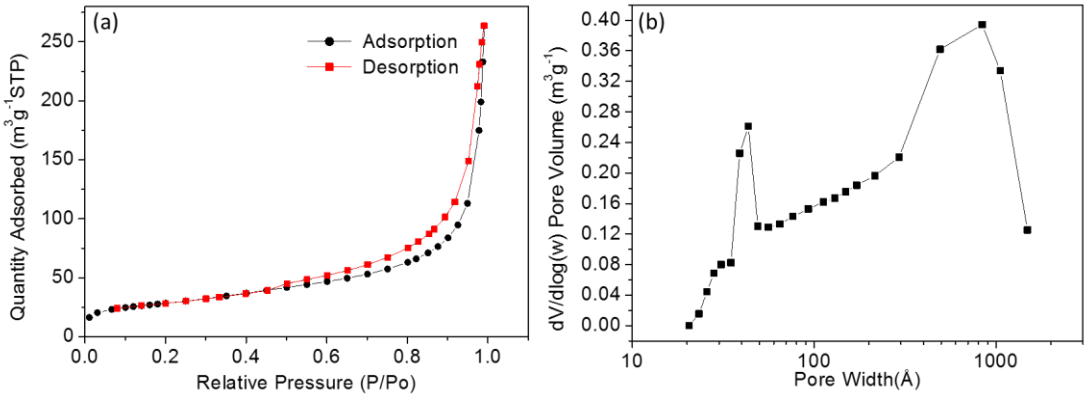

Figure 34. (a) Nitrogen sorption isotherms of $Co_xNi_{1-x}(OH)_2$; (b) Pore size distribution.

As shown in Figure 35, The $Co_xNi_{1-x}(OH)_2$: Pt material maintains the nanosheet morphology of the $Co_xNi_{1-x}(OH)_2$ precursor. However, some tiny white particles were observed on the surface of $Co_xNi_{1-x}(OH)_2$ nanosheets which suggesting the present of Pt particles.

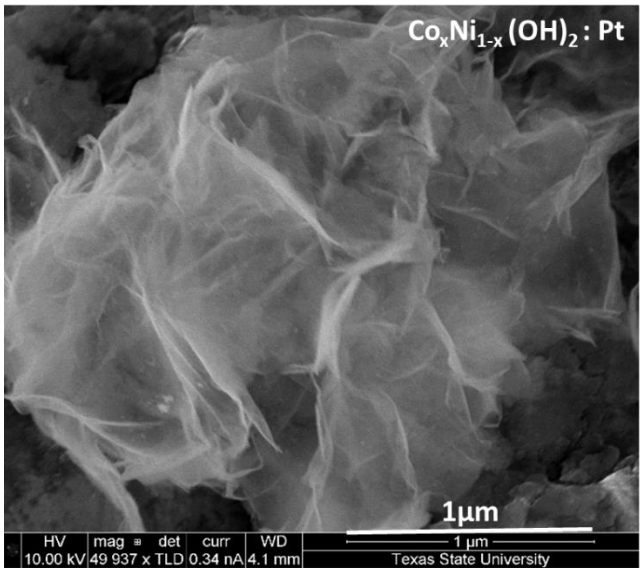

Figure 35. SEM image of $Co_xNi_{1-x}(OH)_2$ nanosheets deposited with Pt.

As observed from Figure 36(a), after thermal treatment, the catalyst exhibits a 2D nanoframe architecture with an interconnected network of solid and pores. Particularly, the catalyst exhibits some particles morphology which may be some metallic(Co/Ni) particles. The process of the metal hydroxide reduction is accompanied by the formation of nuclei of metallic Co/Ni particles and the merging of the metallic particles[73, 79], thus the catalyst shows the particle morphology. Shown in Figure 36 (b-d) are EDS mapping images of the Co-Ni-Pt-200, Co, Ni and Pt are homogeneously distributed on the catalyst. In addition, the present of around 20% of oxygen element indicates that the metal

hydroxide may not completely transform to metallic Co/Ni, some oxide phases are present in the synthesized sample.[73]

The adsorption-desorption isotherms plot of Co-Ni-Pt-200 nanosheets is shown in Figure 37 (a), and exhibit the type II characteristic hysteresis loop which indicated the present of mesopores. Thermally treated samples exhibit BET surface area of 64.9 m^2/g which is smaller than $Co_xNi_{1-x}(OH)_2$. Figure 37(b). shows the pore volume and size distribution of the mesopores. The catalyst demonstrates an increase in pore volume with a peak around 100 nm.

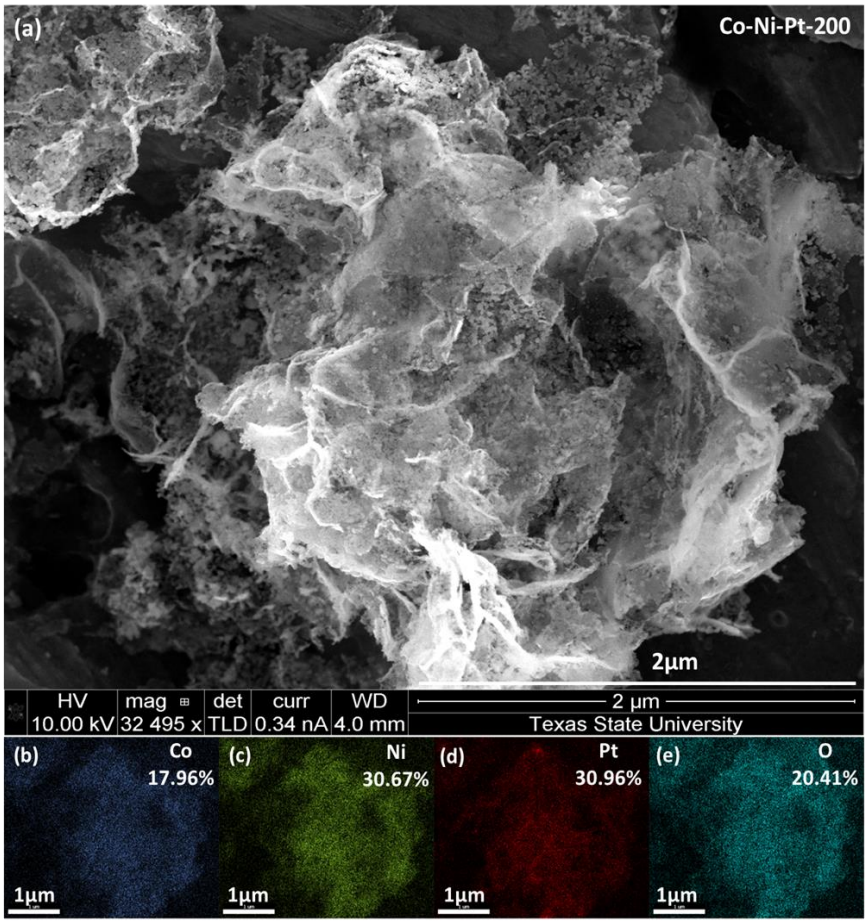

Figure 36. (a) SEM image of Co-Ni-Pt-200; (b-c) EDS elemental mapping.

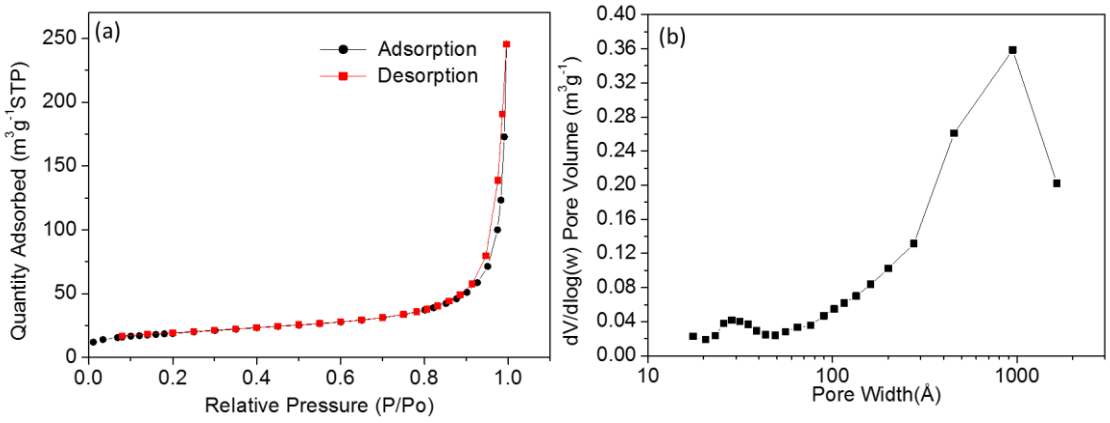

Figure 37. (a) Nitrogen sorption isotherms of Co-Ni-Pt-200; (b) Pore size distribution.

It has been reported that the α-$Co(OH)_2$ and α-$Ni(OH)_2$ have similar XRD pattern.[84] In Figure 38, the XRD pattern of the $Co_xNi_{1-x}(OH)_2$ nanosheets exhibited reflections at 2θ values of 10.8° and 33.7° which can be indexed as (001) and (100) crystal planes of α-$Co(OH)_2$ and α-$Ni(OH)_2$ phase, respectively. The diffraction peak of (001) plane of $Co_xNi_{1-x}(OH)_2$ is much stronger than the others which suggests that the (001) is preferential orientation of $Co_xNi_{1-x}(OH)_2$ growth. The $Co_xNi_{1-x}(OH)_2$ exhibits a larger interlayer spacing (8.13Å) than α-$Co(OH)_2$ (7.30Å).

After Pt deposition, the XRD of $Co_xNi_{1-x}(OH)_2$: Pt shown no distinct peaks of Pt. However, the elemental mapping of the Co-Ni-Pt-200 demonstrated that Pt is present. Therefore, Pt may have very poor crystallinity or an amorphous structure. The new peak shows in 21.8° may be related to the cobalt oxyhydroxide (standard JCPDS card No. 01-073-1213) which has diffraction peaks at 2θ=20.2° corresponding to the (003) plane.

After thermal treatment, the Co-Ni-Pt-200 sample did not present diffraction peaks associated with α-$Co(OH)_2$ or α-$Ni(OH)_2$. The peak at 2θ=43.1° may be related to

Co (111) of 2θ=44.2° or Ni (111) of 2θ=44.5° which is consistence with the magnetic feature of Co-Ni-Pt-200 shown in Figure 39. However, it shifts to a lower 2θ values suggests a Pt-Co/Ni alloy phase. In addition, the sample shows XRD peak corresponding to Pt-fcc: (111). As shown in Table 5, the Pt (111) diffraction peaks of 2θ=40.6° for Co-Ni-Pt-200 is slightly shifted to higher 2θ degree when compared with commercial Pt/C-Etek (39.5°) which supports that the Pt lattice distance was altered by incorporation of Co and Ni.

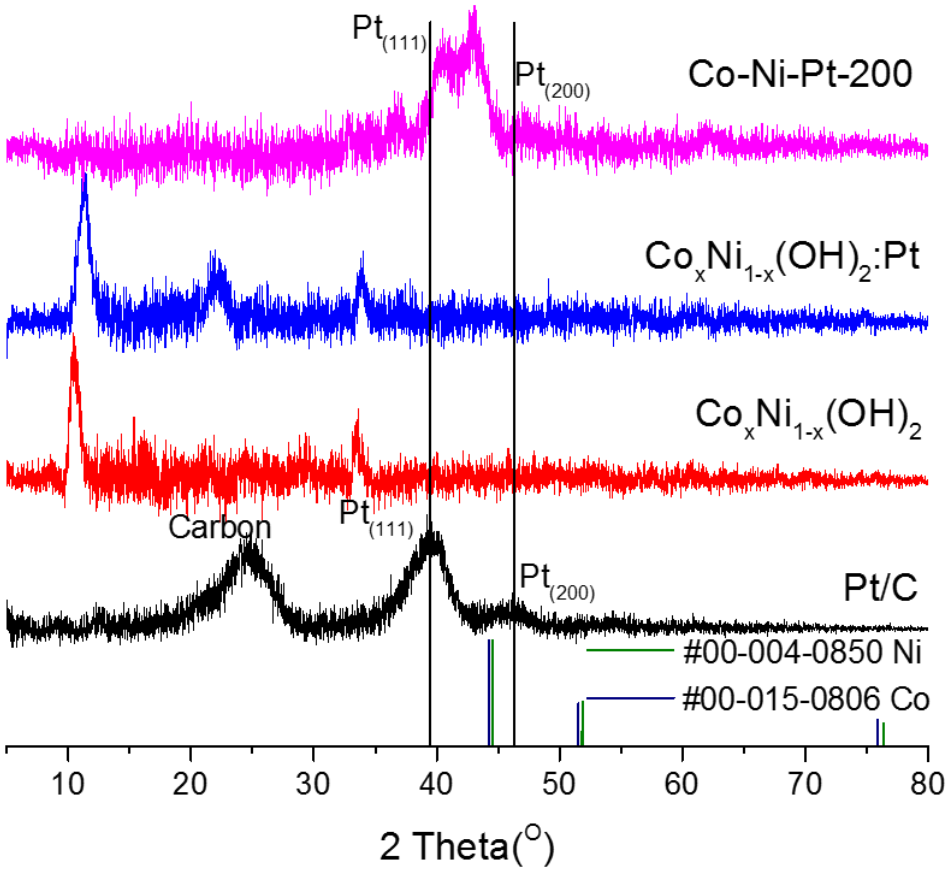

Figure 38. XRD of $Co_xNi_{1-x}(OH)_2$, $Co_xNi_{1-x}(OH)_2$:Pt, Co-Ni-Pt-200 and their corresponding references: Co, Ni and Pt/C.

Figure 39. Magnetic feature of Co-Ni-Pt-200.

Table 5. Comparison of interlayer spacing of Pt in Pt/C, Co-Pt-200 and Co-Ni-Pt-200.

Sample ID	**Pt(2Θ)**	**Pt(Å) (111)**	**Pt(2Θ)**	**Pt(Å) (200)**
Pt/C	39.5	2.28	46.3	1.96
Co-Pt-200	40.2	2.24	46.7	1.94
Co-Ni-Pt-200	40.5	2.22	-	-

3.4.2 Electrochemical Surface Area and Oxygen Reduction Reaction Activity of Ternary Co-Ni-Pt Alloy

Figure 40(a) shows the CV curves of Co-Ni-Pt-200, Co-Pt-200 and Pt/C in N_2-saturated 0.1 M $HClO_4$ solution. After the electrochemical activation, the voltammograms showed polycrystalline platinum profiles similar with that of the Pt/C.

Compared with Pt/C, the Pt oxidation and reduction peaks of Co-Ni-Pt-200 catalysts have positive shifts of ~35 mV which is consistent with the trend of altered electronic structures of these alloys.[16]

Figure 40(b) shows the electrochemical CO oxidation (CO stripping) curves of catalysts with different temperature treatment and Pt/C between 0.6 and 1.0 V_{RHE} after subtraction of the second scan. The thermal treatment catalysts display CO stripping peaks at lower potentials (0.68V) compared with commercial Pt/C (0.79 V).

As shown in Table 6, the calculated $ECSA_{Pt,\ Hupd}$ and $ECSA_{Pt,\ CO}$ of the catalysts are decreased with the interaction of Ni. As the BET surface area of Co-Ni-Pt-200 are larger than Co-Pt-200 and weight ratio of Pt element (based on EDS mapping) of Co-Ni-Pt-200 are similar with Co-Pt-200, the decreasing of ECSA may due to part of Pt is below the surface region. The experimental $Q_{CO}/2Q_H$ ratio of the thermal treatment catalysts are around 1 which is consistent with a Pt-skeleton arrangement ($Q_{CO}/2Q_H$ = 1)[89].

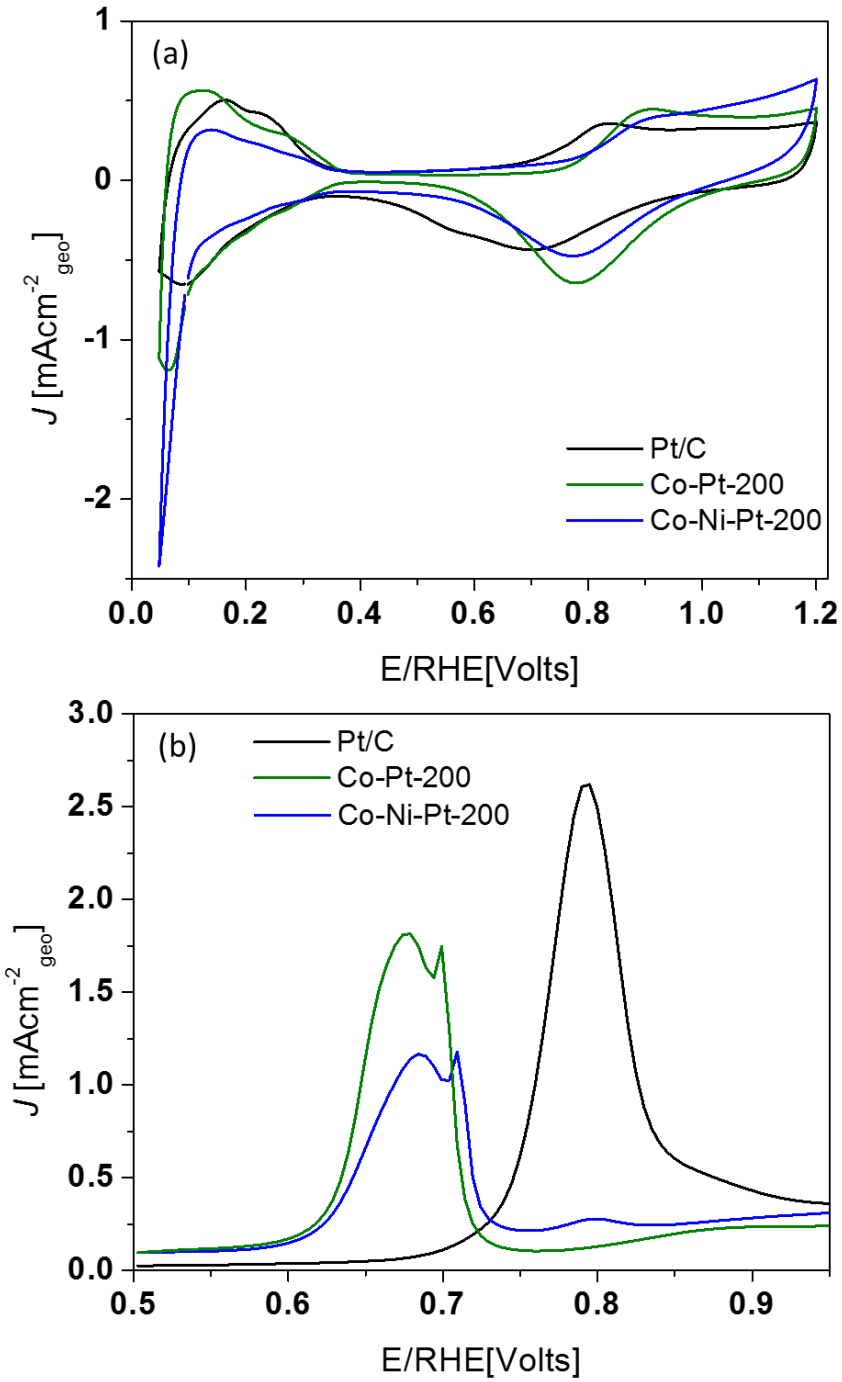

Figure 40. Electrochemistry of Co-Pt-200, Co-Ni-Pt-200 and commercial Pt/C; (a) cyclic voltammetry (electrolyte 0.1 M $HClO_4$ Ar-saturated, scan rate: 20 mV s^{-1}); (b) carbon monoxide (CO) stripping voltammetry. Platinum loadings were L_{Pt}= 26.3 µg cm^{-2}_{geo} (Pt/C), 25 µg cm^{-2}_{geo} (Co-Pt-200) and 23.9 µg cm^{-2}_{geo} (Co-Ni-Pt-200).

Table 6. Comparison of the platinum electrochemical surface area ($ECSA_{Pt}$) from CO stripping ($ECSA_{Pt,CO}$) and H_{upd} regions ($ECSA_{Pt,Hupd}$) and the ratio of $ECSA_{Pt}$ from CO stripping and H_{upd} regions of Pt/C, Co-Pt-200 and Co-Ni-Pt-200.

Catalyst	**$ECSA_{Pt, CO}$ ($m^2\ g^{-1}Pt$)**	**$ECSA_{Pt, Hupd}$ ($m^2\ g^{-1}Pt$)**	**Ratio $ECSA_{Pt, CO}$ / $ECSA_{Pt, Hupd}$ ($Q_{CO}/2Q_H$)**
Pt/C	75.4	72.1	1.04
Co-Pt-200	23.4	24.9	0.94
Co-Ni-Pt-200	16.9	16.2	0.96

Figure 41(a) shows the hydrodynamic polarization curves of Co-Ni-Pt-200, Co-Pt-200 and Pt/C. Co-Ni-Pt-200 shows better catalytic activity toward the ORR than the Pt/C catalyst, however it is worse than Co-Pt-200. Also, the onset potential and the half-wave potential are between Pt/C and the Co-Pt-200. As shown in Figure 41 (b, c), the Co-Ni-Pt-200 shows specific activities at 0.9 V_{RHE} of 4.6 mA $cm^{-2}{}_{Pt}$ and the mass activity is 1.2 A $mg^{-1}{}_{Pt}$.

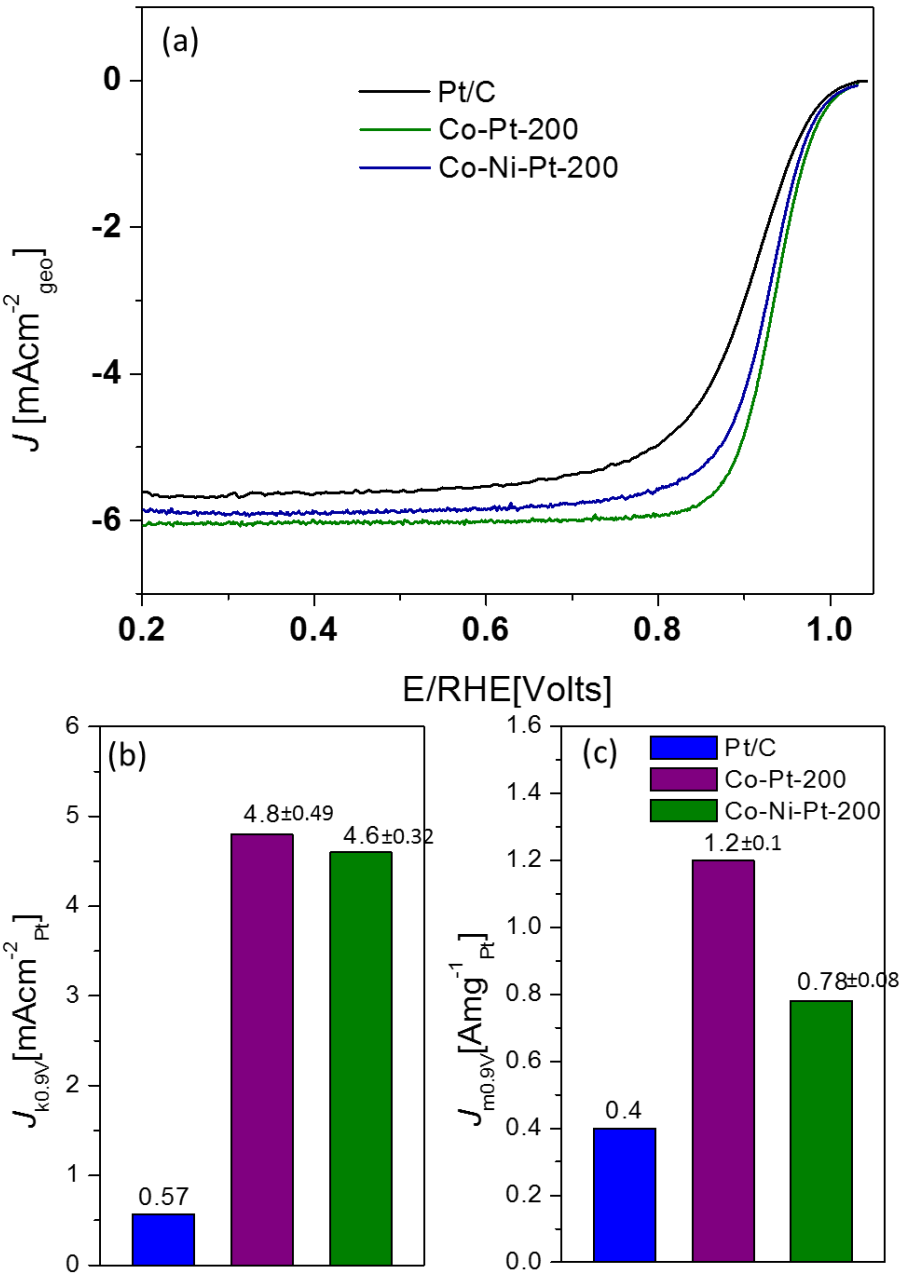

Figure 41. Electrochemistry of Co-Pt-200, Co-Ni-Pt-200 and commercial Pt/C; (a) Potentiodynamic scans in ORR region (electrolyte 0.1 M $HClO_4$ O_2-saturated, scan rate: 20 mV s^{-1}, 1600 rpm); (b) comparison of ORR specific activities and (c) mass-normalized activities at 0.9 V_{RHE}. Platinum loadings were L_{Pt}= 26.3 µg cm^{-2}_{geo} (Pt/C), 25 µg cm^{-2}_{geo} (Co-Pt-200) and 23.9 µg cm^{-2}_{geo} (Co-Ni-Pt-200).

As shown in Figure 7, compared with reported Pt-M (M=Co, Ni, Cu and Mo) catalysts, the Co-Pt-200 2D nanoframes ORR catalyst showed one of the highest ORR specific and mass activity of unsupported and carbon-supported catalysts reported to date.

Table 7. Comparison of specific activities and mass activities of Pt-M (M=Ni, Co, other) ORR catalysts.

Support	**Composition**	**Catalyst Material Details**	**Specific Activity(SA)**		**Mass Activity(MA)**		**Ref.**
			SA ($mAcm^{-2}_{Pt}$)	**Voltage (V_{RHE})**	**MA ($A\ mg^{-1}_{Pt}$)**	**Voltage (V_{RHE})**	
Unsupported (Carbon free)	Pt-Co	Co-Pt-200 2D nanoframe	4.8±0.49	0.90	1.2±0.1	0.90	This work
	Pt-Co	Co-Pt-300 2D nanoframe	4.2±0.95	0.90	0.85±0.15	0.90	
	Pt-Co	Co-Pt-400 2D nanoframe	3.9±0.3	0.90	0.78±0.12	0.90	
	Pt-Co-Ni	Co-Ni-Pt-200 2D nanoframe	4.6±0.32	0.90	0.78±0.08	0.90	
Unsupported (Carbon free)	Pt-Ni	Pt-Ni_3 nanoporosity	2.80	0.90	0.75	0.90	99
	Pt-Co	Pt-Co alloy nanoclusters	0.69	0.90	-	-	61
	Pt-Co	Dealloyed Pt-Co	0.804	0.90	0.38	0.90	100
	Pt-Ni-Co	Pt_3NiCo Pt skin	1.75	0.95	-	-	65
	Pt-Cu	Pt-Cu alloys	0.710	0.90	-	-	101
Carbon supported	Pt-Ni/C	Pt_3Ni nanoframes/C	1.5	0.95	-	-	102
	Pt-Ni/C	$Pt_{2.5}Ni$ octahedra/C	7.3	0.90	-	-	103
	Pt-Co/C	$Co_{15}Pt_{85}$/C Nanocrystal	0.95	0.90	0.80	0.90	104
	Pt-Co/C	Pt_3Co/C ordered nanoparticles	1.10	0.90	0.52	0.90	44
	Pt-Ni-Co/C	$Pt_{20}Ni_{60}Co_{20}$	0.326	0.90	0.472	0.90	94
	Pt-Ni-Co/C	$Pt_{36}Ni_{15}Co_{49}$/C nanoparticles	1.85	0.90	0.88	0.90	105
	Pt-Ni-Mo/C	Mo-Pt_3Ni octahedra/C	10.3	0.90	-	-	106
Extended surfaces	Pt-Ni	Pt_3Ni alloy surfaces	3.0	0.90	-	-	51

4. CONCLUSIONS

α-$Co(OH)_2$ nanosheets were synthesized using a rapid microwave synthesis. The nanosheets showed a BET surface area of 78.4 m^2/g and a large interlayer spacing of 7.30 Å. Deposition of Pt onto the α-$Co(OH)_2$ nanosheets was conducted using a microwave-assisted process. After Pt deposition, heat treatments under reducing conditions were performed to transform α-$Co(OH)_2$ to Co and enable interaction between Co and Pt which is supported by the shifting of XRD diffraction peaks of Pt (111) to higher values compared with values within commercial Pt/C. The Co-Pt catalysts showed significantly lower CO stripping voltages compared with Pt/C which supports the surface electronic is altered compared with Pt/C. The Co-Pt alloy annealed at 200°C showed ORR specific activities at 0.9 V_{RHE} of 4.8 mA cm^{-2}_{Pt} which is 8 times higher than Pt/C. The mass activity was determined to be 1.2 A mg^{-1}_{Pt} which is 3 times higher than Pt/C. Compared with reported values for Pt-Co catalysts, Co-Pt-200 2D nanoframe ORR catalyst showed the highest ORR specific and mass activity of unsupported and carbon-supported Pt-Co catalysts reported to date.

As the treatment temperature treatment increased from 200 °C to 400°C, the BET surface area of the Co-Pt alloy decreased. The ORR catalytic activities of Co-Pt-300 and Co-Pt-400 for ORR were also lower compared with Co-Pt-200 which is attributed to the different electronic structure as supported by the lower voltages for CO stripping.

The effect of introducing a third element, Ni, into Co-Pt system was also studied. The BET surface area of $Co_xNi_{1-x}(OH)_2$ was 99.6 m^2/g. However, the Co-Ni-Pt-200 catalyst showed a lower ECSA supporting a lower amount of Pt atoms at the surface region. The Co-Ni-Pt-200 catalyst also showed lower ORR activity compared to Co-Pt-

200. Further studies are needed to (i) understand the surface atomic and electronic structure; (ii) evaluate the long-term stability of Co-Pt alloy catalysts; and (iii) optimize the thermal treatment parameters to improve the catalytic activity.

LITERATURE CITED

1. Gabbasa, M.; Sopian, K.; Yaakob, Z.; Faraji Zonooz, M.; Fudholi, A.; Asim, N. Review of the energy supply status for sustainable development in the organization of islamic conference. *Renew Sustain Energy Rev*. **2013**, 28, 18-28.
2. Ahuja, D; Tatsutani, M. Sustainable energy for developing countries. *A report to (TWAS) Academy of Sciences for the Developing World*. **2008**, 2, P1-P16.
3. Kong, F.; Zhang, S.; Yin, G.; Zhang, N.; Wang, Z.; Du, C. Pt/porous-IrO_2 nanocomposite as promising electrocatalyst for unitized regenerative fuel cell. *Electrochem. Commun*. **2012**, 14, 63-66.
4. Yao, W.; Yang, J.; Wang, J.; Nuli, Y. Chemical deposition of platinum nanoparticles on iridium oxide for oxygen electrode of unitized regenerative fuel cell. *Electrochem. Commun*. **2007**, 9, 1029-1034.
5. Larminie, J.; Dicks, A. Fuel cell systems explained. Wiley, **2003**.
6. Cheng, F.; Chen, J. Metal-air batteries: From oxygen reduction electrochemistry to cathode catalysts. *Chem. Soc. Rev*. **2012**, 41, 2172-2192.
7. Spendelow, J. S.; Wieckowski, A. Electrocatalysis of oxygen reduction and small alcohol oxidation in alkaline media. *Phys. Chem. Chem. Phys*. **2007**, 9, 2654-2675.
8. Zinola, C.; Arvia, A.; Estiu, G.; Castro, E. A quantum chemical approach to the influence of platinum surface structure on the oxygen electroreduction reaction. *J. Phys. Chem*. **1994**, 98, 7566-7576.
9. Yeager, E. Dioxygen electrocatalysis: Mechanism in relation to catalyst structure. *J. Mol. Catal*. **1986**, 38, 5-25.

10. Cao, R.; Lee, J.S.; Liu, M.; Cho, J. Recent progress in non-precious catalysts for metal-air batteries. *Adv. Energy Mater*. **2012**, 2, 816-829.
11. Vesborg, P. C. K.; Jaramillo, T. F. Addressing the terawatt challenge: Scalability in the supply of chemical elements for renewable energy. *RSC Adv*. **2012**, 2 (21), 7933-7947.
12. Markovic, N.M.; Ross, P.N. Surface science studies of model fuel cell electrocatalysts. *Surf. Sci. Rep*. **2002**, 45, 117-229.
13. Hoare, JP. The electrochemistry of oxygen. New York: Wiley, **1968**.
14. Wkabayashi, N.; Takeichi, M; Itagaki, M.; Uchida, H.; Watanabe, M. Temperature dependence of oxygen reduction activity at a platinum electrode in an acidic electrolyte solution investigated with a channel flow double electrode. *J. Electroanal. Chem*. **2005**, 574, 339-46.
15. Stassi, A.; D'Urso, C.; Baglio, V.; Di Blasi, A.; Antonucci, V.; Arico A.S.; Castro Luna, A.M.; Bonesi, A.; Triaca, W.E. Electrocatalytic behaviour for oxygen reduction reaction of small nanostructured crystalline bimetallic Pt-M supported catalysts. *J. Appl. Electrochem*. **2006**, 36, 1143-1149.
16. Stamenkovic, V. R.; Mun, B. S.; Arenz, M.; Mayrhofer, K. J. J.; Lucas, C. A.; Wang, G.; Ross, P. N.; M. Markovic, N. Trends in electrocatalysis on extended and nanoscale Pt-bimetallic alloy surfaces. *Nature Materials*. **2007**, 6, 241-247.
17. Stephens, I. E. L.; Bondarenko, A. S.; Gronbjerg, U.; Rossmeisl, J.; Chorkendorff, I. Understanding the electrocatalysis of oxygen reduction on platinum and its alloys. *Energy Environ. Sci*. **2012**, 5 (5), 6744-6762.

18. Jia, Q.; Liang, W.; Bates, M. K.; Mani, P.; Lee, W.; Mukerjee, S. Activity descriptor identification for oxygen reduction on Pt-based bimetallic nanoparticles: In situ observation of the linear Composition-Strain-Activity relationship. *ACS Nano*. **2015**, 9 (1), 387-400.
19. Hwang, S. J.; Kim, S.K.; Lee, J.G.; Lee, S.C.; Jang, J. H.; Kim, P.; Lim, T.H.; Sung, Y.E.; Yoo, S. J. Role of electronic perturbation in stability and activity of Pt-based alloy nanocatalysts for oxygen reduction. *J. Am. Chem. Soc*. **2012**, 134 (48), 19508-19511.
20. Xin, H.; Vojvodic, A.; Voss, J.; Nørskov, J. K.; Abild-Pedersen1, F. Effects of d-band shape on the surface reactivity of transition-metal alloys. *Physical Review B.* **2014**, 89, 115114.
21. Kuzume, A.; Herrero, E.; Feliu, J. M. Oxygen reduction on stepped platinum surfaces in acidic media. *J. Electroanal. Chem*. **2007**, 599 (2), 333-343.
22. Gomez-Marín, A. M.; Rizo, R.; Feliu, J. M. Some reflections on the understanding of the oxygen reduction reaction at Pt (111). *Beilstein J. Nanotechnol*. **2013**, 4, 956-967.
23. Stamenkovic, V. R.; Mun, B. S.; Arenz, M.; Mayrhofer, K. J. J.; Lucas, C. A.; Wang, G.; Ross, P. N.; Markovic, N. M. Trends in electrocatalysis on extended and nanoscale Pt-bimetallic alloy surfaces. *Nat. Mater*. **2007**, 6, 241-247.
24. Kitchin, J. R.; Nørskov, J. K. Role of strain and ligand effects in the modification of the electronic and chemical properties of bimetallic surfaces. *Phys. Rev. Lett*. **2004**, 93, 156801-156804.

25. Bligaard, T.; Nørskov, J. K. Ligand effects in heterogeneous catalysis and electrochemistry. *Electrochim. Acta*. **2007**, 52, 5512-5516.

26. Strasser, P.; Koh, S.; Anniyev, T.; Greeley, J.; More, K.; Yu, C. F.; Kaya, S.; Nordlund, D.; Ogasawara, H.; Nilsson, A. Lattice-strain control of the activity in dealloyed core-shell fuel cell catalysts. *Nat. Chem*. **2010**, 2, 454-460.

27. Stamenkovic, V.; Mun, B. S.; Mayrhofer, K. J. J.; Ross, P. N.; Markovic, N. M.; Rossmeisl, J.; Greeley, J.; Nørskov, J. K. Changing the activity of electrocatalysts for oxygen reduction by tuning the surface electronic structure. *Angew. Chem. Int. Ed*. **2006**, 45, 2897-2901.

28. Stamenkovic, V.; Schmidt, T. J. Surface composition effects in electrocatalysis: kinetics of oxygen reduction on well-defined Pt_3Ni and Pt_3Co alloy surfaces. *J. Phys. Chem. B*. **2002**, 106, 11970-11979.

29. Wang, C.; Markovic, N. M.; Stamenkovic, V. R. Synthesis of homogeneous Pt-bimetallic nanoparticles as highly efficient electrocatalysts. *ACS Catal*. **2011**, 1, 1355-1359.

30. Toda, T.; Igarashi, H.; Uchida, M.; Watanabe, M. Enhancement of the electroreduction of oxygen on Pt alloys with Fe, Ni, and Co. *J. Electrochem. Soc*. **1999**, 146, 3750-3756.

31. Bode, H.; Dehmelt, K.; Witte, J. Zur kenntnis der Nickelhydroxidelektrode-I.Über das Nickel(II)-hydroxidhydrat. *Electrochim. Acta*. **1966**, 11, 1079-1087.

32. Hall, D.S.; Lockwood, D.J.; Poirier, S.; Bock, C.; MacDougall, B.R. Raman and infrared spectroscopy of α and β phases of thin nickel hydroxide films electrochemically formed on nickel. *J. Phys. Chem. A*. **2012**, 116, 6771-6784.

33. Jeevanandam, P.; Koltypin, Y.; Gedanken, A. Synthesis of nanosized α-nickel hydroxide by a sonochemical method. *Nano Lett*. **2001**, 1, 263-266.

34. Dennstedt, W.; Löser, W. Zur kenntnis der nickelhydroxid-elektrode-III. thermogravimetrische untersuchungen an Nickel(II)-hydroxiden. *Electrochim. Acta*. **1971**,16, 429-435.

35. Zhu, Z.; Wei, N.; Liu, H.; He, Z. Microwave-assisted hydrothermal synthesis of $Ni(OH)_2$ architectures and their in situ thermal convention to NiO. *Adv. Powder Technol*. **2011**, 22, 422-426.

36. Xu, L.; Ding, Y.S.; Chen, C.H.; Zhao, L.; Rimkus, C.; Joesten, R.; Suib, S.L. 3D flowerlike α-nickel hydroxide with enhanced electrochemical activity synthesized by microwave-assisted hydrothermal method. *Chem. Mater*. **2007**, 20, 308-316.

37. Garland Nancy, L. 2008 DOE Hydrogen program merit review and peer evaluation meeting, Arlington, Washington, DC, **2008**.

38. Xia, Y.; Yang, P.; Sun, Y.; Wu, Y.; Mayers, B.; Gates, B.; Yin, Y.; Kim, F.; Yan, H. One-dimensional nanostructures: Synthesis, characterization, and applications. *Adv. Mater*. **2003**, 15, 353.

39. Wang, Y. J.; Wilkinson, D. P.; Zhang, J.J. Noncarbon support materials for polymer electrolyte membrane fuel cell electrocatalysts. *J. Chem. Rev*. **2011**, 111, 7625-7651.

40. Fang, B.; Kim, M.; Kim, J.; Song, M.; Wang, Y.; Wang, H.; Wilkinson, D.; Yu, J. High Pt loading on functionalized multiwall carbon nanotubes as a highly efficient cathode electrocatalyst for proton exchange membrane fuel cells. *J. Mater. Chem.* **2011**, 21, 8066-8073.

41. Trogadas, P.; Fuller, T. F.; Strasser, P. Carbon as catalyst and support for electrochemical energy conversion. *Carbon*. **2014**, 75, 5-42.

42. Kou, R.; Shao, Y.; Mei, D.; Nie, Z.; Wang, D.; Wang, C.; Viswanathan, V. V.; Park, S.; Aksay, I. A.; Lin, Y.; Wang, Y.; Liu, J. Stabilization of electrocatalytic metal nanoparticles at metal-metal oxide-graphene triple junction points. *J. Am. Chem. Soc*. **2011**, 133, 2541-2547.

43. Wu, J.; Yuan, X.-Z.; Martin, J. J.; Wang, H.; Zhang, J.; Shen, J.; Wu, S.; Merida, W. A review of PEM fuel cell durability: Degradation mechanisms and mitigation strategies. *J. Power Sources*. 2008, 184, 104-119.

44. Wang, D.; Xin, H. L.; Hovden, R.; Wang, H.; Yu, Y.; Muller, D. A.; Disalvo, F. J.; Abruña, H. D. Structurally ordered intermetallic platinum-cobalt core-shell nanoparticles with enhanced activity and stability as oxygen reduction electrocatalysts. *Nat. Mater*. **2013**, 12, 81-87.

    Xiong, L.; Manthiram, A. Nanostructured Pt-M/C (M=Fe and Co) catalysts prepared by a microemulsion method for oxygen reduction in proton exchange membrane fuel cells. *Electrochim. Acta*. **2005**, 50, 2323-2329.

45. Shao, Y.; Liu, J.; Wang, Y.; Lin, Y. Novel catalyst support materials for PEM fuel cells: current status and future prospects. *J. Mater. Chem*. **2009**, 19, 46-59.

46. Zhou, J. G.; Zhou, X. T.; Sun, X. H.; Li, R. Y.; Murphy, M.; Ding, Z. F.; Sun, X. L.; Sham, T. K. Interaction between Pt nanoparticles and carbon nanotubes-An X-ray absorption near edge structures (XANES) study. *Chem. Phys. Lett*. **2007**, 437, 229-232.

47. Adzic, R. R.; Zhang, J.; Sasaki, K.; Vukmirovic, M. B.; Shao, M.; Wang, J. X.; Nilekar, A. U.; Mavrikakis, M.; Valerio, J. A.; Uribe, F. Platinum monolayer fuel cell electrocatalysts. *Top. Catal*. **2007**, 46, 249-262.

48. Stamenkovic, V.; Schmidt, T. J.; Ross, P. N.; Markovic, N. M. Surface composition effects in electrocatalysis: Kinetics of oxygen reduction on well-defined Pt_3Ni and Pt_3Co alloy surfaces. *J. Phys. Chem. B*. **2002**, 106, 11970-11979.

49. Stamenkovic, V.; Schmidt, T. J.; Ross, P. N.; Markovic, N. M. Surface segregation effects in electrocatalysis: Kinetics of oxygen reduction reaction on polycrystalline Pt_3Ni alloy surfaces. *J. Electroanal. Chem*. **2003**, 554, 191-199.

50. Stamenkovic, V. R.; Mun, B. S.; Mayrhofer, K. J. J.; Ross, P. N.; Markovic, N. M. Effect of surface composition on electronic structure, stability, and electrocatalytic properties of Pt-transition metal alloys: Pt-skin versus Pt-skeleton surfaces. *J. Am. Chem. Soc*. **2006**, 128, 8813-8819.

51. Stamenkovic, V. R.; Mun, B. S.; Arenz, M.; Mayrhofer, K. J. J.; Lucas, C. A.; Wang, G.; Ross, P. N.; Markovic, N. M. Trends in electrocatalysis on extended and nanoscale Pt-bimetallic alloy surfaces. *Nat. Mater*. **2007**, 6, 241-247.

52. Chrzanowski, W.; Wieckowski, A. Ultrathin films of ruthenium on low index Platinum single crystal surfaces: An electrochemical study. *Langmuir*. **1997**, 13, 5974-5978.

53. Antolini, E.; Gonzalez, E. R. Ceramic materials as supports for low-temperature fuel cell catalysts. *Solid State Ionics*. **2009**, 180, 746-763.

54. Evans, S. A. G.; Terry, J. G.; Plank, N.; Walton, A.; Keane, L.; Campbell, C.; Ghazal, P.; Beattie, J.; Su, T.; Crain, J.; Mount, A. Electrodeposition of platinum metal on TiN thin films. *Electrochem. Commun*. **2005**, 7, 125-129.

55. Krawiec, P.; Kaskel, S. Thermal stability of high surface area silicon carbide materials. *J. Solid State Chem*. **2006**, 179, 2281-2289.

56. Feng, Y.; Yao, R.; Zhang, L. Electronic properties of nanocrystalline tin oxide dispersed in monolithic mesoporous silica. *Physica. B*. **2004**, 350, 348-352.

57. Rajesh, K.; Ahuja, T.; Kumar, D. Recent progress in the development of nano-structured conducting polymers/nanocomposites for sensor applications. *Sens. Actuators, B*. **2009**, 136, 275-286.

58. Bing, Y.; Liu, H.; Zhang, L.; Ghosh, D.; Zhang, J. Nanostructured Pt-alloy electrocatalysts for PEM fuel cell oxygen reduction reaction. *Chem. Soc. Rev*. **2010**, 39, 2184-2202.

59. Chen, Z. W.; Waje, M.; Li, W. Z.; Yan, Y. S. Supportless Pt and PtPd nanotubes as electrocatalysts for oxygen-reduction reactions. *Angew. Chem. Int. Ed*. **2007**, 46, 4060-4063.

60. Baldizzone, C.; Gan, L.; Hodnik, N.; Keeley, G. P.; Kostka, A.; Heggen, M.; Strasser, P.; Mayrhofer, K. J. J. Stability of dealloyed porous Pt/Ni nanoparticles. *ACS Catal*. **2015**, 5, 5000-5007.

61. Narayanamoorthy, B.; Linkov, V.; Sita, C.; Pasupathi, S. Pt_3M (M: Co, Ni and Fe) bimetallic alloy nanoclusters as support-free electrocatalysts with improved activity and durability for dioxygen reduction in PEM fuel cells. *Electrocatalysis*. **2016**, 7, 400-410.

62. Huang, J.; Liu, Q.; Yao, T.; Pan, Z.; Wei, S.16th International conference on X-ray absorption fine structure (XAFS16).

63. Mukerjee, S.; Srinivasan, S.; Soriaga, M. P.; McBreen, J. Role of structural and electronic properties of Pt and Pt alloys on electrocatalysis of oxygen reduction an in situ XANES and EXAFS investigation. *Electrochem. Soc*. **1995**, 142, 1409-1422.

64. Huang, J., Chen, J., Yao, T., He, J., Jiang, S., Sun, Z., Liu, Q., Cheng, W., Hu, F., Jiang, Y., Pan, Z., Wei S. CoOOH nanosheets with high mass activity for water oxidation. *Angew. Chem. Int. Ed. Engl*. **2015**, 54, 8722-8727.

65. Wang, C.; Li, D.; Chi, M.; Pearson, J.; Rankin, R. B.; Greeley, J.; Duan, Z.; Wang, G.; van der Vliet, D.; More, K. L.; Markovic, N. M.; Stamenkovic, V. R. Rational development of ternary alloy electrocatalysts. *J. Phys. Chem. Lett*. **2012**, 3, 1668-1673.

66. Aran-Ais, R. M.; Dionigi, F.; Merzdorf, T.; Gocyla, M.; Heggen, M.; Dunin-Borkowski, R. E.; Gliech, M.; Solla-Gullon, J.; Herrero, E.; Feliu, J. M.; Strasser, P. Elemental anisotropic growth and atomic-scale structure of shape controlled octahedral Pt-Ni-Co alloy nanocatalysts. *Nano Lett*. **2015**, 15, 7473-7480.

67. Wang, B.; Chen, J. S.; Wang, Z. Y.; Madhavi, S.; Lou, X. W. Green synthesis of NiO nanobelts with exceptional pseudo-capacitive properties. *Adv. Energy Mater*. **2012**, 2, 1188-1192.

68. Godinez-Salomon, F.; Hallen-Lopez, M.; Solorza-Feria, O. Enhanced electroactivity for the oxygen reduction on Ni@Pt core-shell nanocatalysts. *Int. J. Hydrogen Energy*. **2012**, 37, 14902-14910.

69. Garsany, Y; Baturina, O; Swider-Lyons, K; Kocha, S. Experimental methods for quantifying the activity of Platinum electrocatalysts for the oxygen reduction reaction. *Anal. Chem*. **2010**, 82, 6321-6328.

70. Shinozaki, K.; Zack, J. W.; Richards, R. M.; Pivovar, B. S.; Kocha, S. S. Oxygen reduction reaction measurements on Platinum electrocatalysts utilizing rotating disk electrode technique. *J. Electrochem. Soc*. **2015**, 162, F1144-F1158.

71. Van der Vliet, D.; Wang, C.; Li, D.; Paulikas, Arvydas P. J.; Rankin Greeley, R.; Strmcnik, D.; Tripkovic, D.; Markovic, N. M.; Stamenkovic, V.R. Unique electrochemical adsorption properties of Pt-skin surfaces. *Angew. Chem. Int. Ed*. **2012**, 51, 3139-3142.

72. Markovic, N. M.; Gasteiger, H. A.; Grgur, B. N.; Ross, P. N. Oxygen reduction reaction on Pt (111): effects of bromide. *J. Electroanal. Chem.* **1999**, 467, 157-163.

73. Tikhomirov, S. A.; Alymov, M. I.; Tregubova, I. V.; Shustov, V. S. Influence that Cobalt hydroxide reduction regimes have on dispersion and reduction degree of Cobalt nanopowders. *Nanotechnologies in Russia*. **2011**, 6, 268-271.

74. Kasai, A.; Fujihara, S. Layered single-metal hydroxide/ethylene glycol as a new class of hybrid material. *Inorg. Chem*. **2006**, 45, 415-418.

75. Wang, C.; Zhang, X.; Xu, Z.; Sun, X.; Ma, Y. Ethylene glycol intercalated Cobalt/Nickel layered double hydroxide nanosheet assemblies with ultrahigh specific capacitance: Structural design and green synthesis for advanced electrochemical storage. *ACS Appl. Mater. Interfaces*. **2015**, 7, 19601-19610.

76. Wang, C.; Zhang, X.; Zhang, D.; Yao, C.; Ma, Y. Facile and low-cost fabrication of nanostructured $NiCo_2O_4$ spinel with high specific capacitance and excellent cycle stability. *Electrochim. Acta.* **2012**, 63, 220-227.

77. Rao, C.; Trivedi, D.C. Chemical and electrochemical depositions of platinum group metals and their applications. *Coordination Chemistry Reviews*. **2005**, 249, 613-631.

78. Kokkinidis, G.; Papoutsis, A.; Stoychev, D.; Milchev, A. Electroless deposition of Pt on Ti-catalytic activity for the hydrogen evolution reaction. *Journal of Electroanalytical Chemistry*. **2000**, 486, 48-55.

79. Sidorova, E. G.; Dzidziguri, E. L.; Levina, V. V.; Ryzhonkov, D. I. Dispersion characteristics of a nickel nanopowder. *Russian Metallurgy (Metally)*. **2008**, 6, 513-517.

80. Yang, J.; Liu, H.; Martens, W. N.; Frost, R. L. Synthesis and characterization of Cobalt hydroxide, Cobalt oxyhydroxide, and Cobalt oxide nanodiscs. *J. Phys. Chem. C*. **2010**, 114, 111-119.

81. Zhang, Y.; Xia, X.; Kang, J.; Tu, J. Hydrothermal synthesized porous $Co(OH)_2$ nanoflake film for supercapacitor application. *Chinese Science Bulletin*. **2012**, 57(32), 4215-4219.

82. Gupta, V.; Kusahara, T.; Toyama, H.; Gupta, S.; Miura, N. Potentiostatically deposited nanostructured α-$Co(OH)_2$: A high performance electrode material for redox-capacitors. *Electrochemistry Communications*. **2007**, 9, 2315-2319.

83. Gourrier, L.; Deabate, S.; Michel, T.; Paillet, M.; Hermet, P.; Bantignies, J.L.; Henn, F. Characterization of unusually large 'pseudo-single crystal' of β-nickel hydroxide. *J. Phys. Chem. C*. **2011**, 115, 15067-15074.

84. Dixit, M.; Subbanna, G. N.; Vishnu Kamath, P. Homogeneous precipitation from solution by urea hydrolysis: a novel chemical route to the α-hydroxides of nickel and cobalt. *J. Muter. Chem*. **1996**, 6(8), 1429-1432.

85. Wang, J. X.; Markovic, N. M.; Adzic, R. R. Kinetic analysis of oxygen reduction on Pt (111) in acid solutions: Intrinsic kinetic parameters and anion adsorption effects. *J. Phys. Chem. B*. **2004**, 108, 4127-4133.

86. van der Vliet, D. F.; Wang, C.; Li, D. G.; Paulikas, A. P.; Greeley, J.; Rankin, R. B.; Strmcnik, D.; Tripkovic, D.; Markovic, N. M.; Stamenkovic, V. R. Unique electrochemical adsorption properties of Pt-skin surfaces. *Angew. Chem*. **2012**, 124, 3193-3196.

87. Strmcnik, D. S.; Tripkovic, D. V.; van der Vliet, D.; Chang, K. C.; Komanicky, V.; You, H.; Karapetrov, G.; Greeley, J.; Stamenkovic, V. R.; Markovic, N. M. Unique Activity of Platinum Adislands in the CO Electrooxidation Reaction. *J. Am. Chem. Soc*. **2008**, 130, 15332-15339.

88. Kuttiyiel, K. A.; Sasaki, K.; Choi, Y.; Su, D.; Liu, P.; Adzic, R. R. Nitride Stabilized PtNi Core-Shell Nanocatalyst for high Oxygen Reduction Activity. Nano Lett. 2012, 12, 6266-6271.

89. Wang, C.; Chi, M. F.; Li, D. G.; Strmcnik, D.; van der Vliett, D.; Wang, G. F.; Komanicky, V.; Chang, K. C.; Paulikas, A. P.; Tripkovic, D.; Pearson, J.; More, K. L.; Markovic, N. M.; Stamenkovic, V. R. Design and Synthesis of Bimetallic Electrocatalyst with Multilayered Pt-Skin Surfaces. *J. Am. Chem. Soc*. **2011**, 133, 14396-14403.

90. Mayrhofer, K. J. J.; Strmcnik, D.; Blizanac, B. B.; Stamenkovic, V.; Arenz, M.; Markovic, N. M. Measurement of oxygen reduction activities via the rotating disc electrode method: From Pt model surfaces to carbon-supported high surface area catalysts. *Electrochim. Acta*, **2008**, 53, 3181-3188.
91. R. Wang, D.C. Higgins, M.A. Hoque, D.U. Lee, F. Hassan, Z. Controlled Growth of Platinum Nanowire Arrays on Sulfur Doped Graphene as High Performance Electrocatalyst. *Scientific Reports 3*, **2013**, Article number: 2431.
92. Mayrhofer, K. J. J.; Strmcnik, D.; Blizanac, B. B.; Stamenkovic, V.; Arenz, M.; Markovic, N. M. Measurement of Oxygen Reduction Activities via the Rotating Disc Electrode Method: From Pt model Surfaces to Carbon-supported High Surface Area Catalysts. *Electrochim. Acta*. **2008**, 53, 3181-3188.
93. Loukrakpam, R.; Chang, P.; Luo, J.; Fang, B.; Mott, D.; Bae, I.T.; Naslund, H. R.; Engelhard, M. H.; Zhong, C. J. Chromium-assisted synthesis of platinum nanocube electrocatalysts. *Chem. Commun*. **2010**, 46(38), 7184-7186.
94. Mani, P.; Srivastava, R.; Strasser, P. Dealloyed binary PtM_3 (M = Cu, Co, Ni) and ternary $PtNi_3M$ (M = Cu, Co, Fe, Cr) electrocatalysts for the oxygen reduction reaction: Performance in polymer electrolyte membrane fuel cells. *Journal of Power Sources*. **2011**, 196, 666-673.
95. Meier, J. C.; Galeano, C.; Katsounaros, I.; Witte, J.; Bongard, H. J.; Topalov, A. A.; Baldizzone, C.; Mezzavilla, S.; Schüth, F.; Mayrhofer, K. Design criteria for stable Pt/C fuel cell catalysts. *Beilstein J Nanotechnol*. **2014**, 5, 44-67.

96. Butler, S. Z.; Hollen, S. M.; Cao, L.; Cui, Y.; Gupta, J. A.; Gutierrez, H. R.; Heinz, T. F.; Huang, J.; Ismach, A. F.; Johnston-Halperin, E.; Kuno, M.; Plashnitsa, V. V.; Robinson, R. D.; Ruoff, R. S.; Salahuddin, S.; Shan, J.; Shi, L.; Spencer, O. M. G.; Terrones, M.; Windl, W.; Goldberger, J. E. Progress, challenges, and opportunities in two-dimensional materials beyond graphene. *Acs Nano*. **2013**, 7, 2898-2926.

97. Godínez-Salomón, F.; Mendoza-Cruz, R.; Arellano-Jimenez, M. J.; Jose-Yacaman, M.; Rhodes, C.P. Metallic two-dimensional nanoframes: Unsupported hierarchical nickel-platinum alloy nanoarchitectures with enhanced electrochemical oxygen reduction activity and stability. *ACS Appl. Mater. Int*. **2017**, 9, 18660-18674.

98. Stamenkovic, V. R.; Fowler, B.; Mun, B. S.; Wang, G. F.; Ross, P. N.; Lucas, C. A.; Markovic, N. M. Improved oxygen reduction activity on Pt_3Ni (111) via increased surface site availability. *Science*. **2007**, 315, 493-497.

99. Gan, L.; Heggen, M.; O'Malley, R.; Theobald, B.; Strasser, P. Understanding and controlling nanoporosity formation for improving the stability of bimetallic fuel cell catalysts. *Nano Lett*. **2013**, 13 (3), 1131-1138.

100. Heggen, M.; Oezaslan, M.; Houben, L.; Strasser, P. Formation and analysis of core-shell fine structures in Pt bimetallic nanoparticle fuel cell electrocatalysts. *J. Phys. Chem. C*. **2012**, 116 (36), 19073-19083.

101. Neergat, M.; Rahul, R., Unsupported Cu-Pt core-shell nanoparticles: Oxygen reduction reaction (ORR) catalyst with better activity and reduced precious metal content. *J. Electrochem. Soc*. **2012**, 159, F234-F241.

102. Chen, C.; Kang, Y. J.; Huo, Z. Y.; Zhu, Z. W.; Huang, W. Y.; Xin, H. L. L.; Snyder, J. D.; Li, D. G.; Herron, J. A.; Mavrikakis, M.; Chi, M. F.; More, K. L.; Li, Y. D.; Markovic, N. M.; Somorjai, G. A.; Yang, P. D.; Stamenkovic, V. R. Highly crystalline multimetallic nanoframes with three-dimensional electrocatalytic surfaces. *Science*. **2014**, 343, 1339-1343.

103. Choi, S. I.; Xie, S. F.; Shao, M. H.; Odell, J. H.; Lu, N.; Peng, H. C.; Protsailo, L.; Guerrero, S.; Park, J. H.; Xia, X. H.; Wang, J. G.; Kim, M. J.; Xia, Y. N. Synthesis and characterization of 9 nm Pt-Ni octahedra with a record high activity of 3.3 A/mg(Pt) for the oxygen reduction reaction. *Nano Lett*. **2013**, 13, 3420-3425.

104. Kakade, B. A.; Wang, H.; Tamaki, T.; Ohashi, H.; Yamaguchi, T. Enhanced oxygen reduction reaction by bimetallic CoPt and PdPt nanocrystals. *RSC Adv*. **2013**, 3 (26), 10487-10496.

105. Wanjala, B. N.; Loukrakpam, R.; Luo, J.; Njoki, P. N.; Mott, D.; Zhong, C.-J.; Shao, M.; Protsailo, L.; Kawamura, T. Thermal treatment of PtNiCo electrocatalysts: effects of nanoscale strain and structure on the activity and stability for the oxygen reduction reaction. *J. Phys. Chem. C*. **2010**, 114 (41), 17580-17590.

106. Huang, X. Q.; Zhao, Z. P.; Cao, L.; Chen, Y.; Zhu, E. B.; Lin, Z. Y.; Li, M. F.; Yan, A. M.; Zettl, A.; Wang, Y. M.; Duan, X. F.; Mueller, T.; Huang, Y. High-performance transition metal-doped Pt_3Ni octahedra for oxygen reduction reaction. *Science*. **2015**, 348, 1230-1234.

107. Mondal, A.K.; Su, D.; Wang, Y.; Chen, S.; Wang, G. Hydrothermal synthesis of nickel oxide nanosheets for lithium-ion batteries and supercapacitors with excellent performance. *Chem. Asian J*. **2013**, 8, 2828-2832.

108. Foelske, A.; Strehblow, H. H. Structure and composition of electrochemically prepared oxide layers on Co in alkaline solutions studied by XPS. *Surf. Interface Anal*. **2002**, 34, 125-129.

109. Diaz, R.; Arbiol, J.; Sanz, F.; Cornet, A.; Morante, J. R. Electroless addition of platinum to SnO_2 nanopowders. *Chem. Mater*. **2002**, 14, 3277-3283.

110. Faure, C.; Delmas, C.; Fouassier, M. Characterization of a turbostratic α-nickel hydroxide quantitatively obtained from an $NiSO_4$ solution. *J. Power Sources*. **1991**, 35, 279-290.

111. Zhang, S.; Zeng, H.C. Self-assembled hollow spheres of β-$Ni(OH)_2$ and their derived nanomaterials. *Chem. Mater*. **2009**, 21, 871-883.

112. Ramesh, T.N.; Kamath, P.V. Synthesis of nickel hydroxide: effect of precipitation conditions on phase selectivity and structural disorder. *J. Power Sources*. **2006**, 156, 655-661.